J. Fluid Mech. (2006), *vol.* 555, *pp.* 1–42.
doi:10.1017/S0022112005008542 Printed in the United Kingdom

Convective instability of electrokinetic flows in a cross-shaped microchannel

By JONATHAN D. POSNER† AND JUAN G. SANTIAGO
Department of Mechanical Engineering, Stanford University, Stanford, CA, USA

(Received 24 February 2005 and in revised form 13 September 2005)

We present a parametric experimental study of convective electrokinetic instability (EKI) in an isotropically etched, cross-shaped microchannel using quantitative epifluorescence imaging. The base state is a three-inlet, one-outlet electrokinetic focusing flow configuration where the centre sample stream and sheath flows have mismatched ionic conductivities. Electrokinetic flows with conductivity gradients become unstable when the electroviscous stretching and folding of conductivity interfaces grows faster than the dissipative effect of molecular diffusion. Scalar images, critical applied fields required for instability, and temporal and spatial scalar energy are presented for flows with a wide range of applied d.c. electric field and centre-to-sheath conductivity ratios. These parameters impose variations of the electric Rayleigh number across four orders of magnitude. We introduce a scaling for charge density in the bulk fluid as a function of local maximum conductivity gradients in the flow. This scaling shows that the flow becomes unstable at a critical electric Rayleigh number ($Ra_{e,\ell} = 205$) and applies to a wide range of applied field and centre-to-sheath conductivity ratios. This work is relevant to on-chip electrokinetic flows with conductivity gradients such as field amplified sample stacking, flow at the intersections of multi-dimensional assays, electrokinetic control and separation of sample streams with poorly specified chemistry, and low-Reynolds number micromixing.

1. Introduction

Chip-based microfluidic devices for micro total analytical systems (μTAS) have been studied extensively over the past fifteen years (see Manz, Graber & Widmer 1990). These systems offer the potential of assays with increased sensitivity and resolution, reduction of sample volume, and integration of multiple laboratory processes and functions on a single platform. Comprehensive reviews of microfabrication, chip designs, sensors, new functionality, and applications for μTAS have been presented (see Vilkner, Janasek & Manz 2004). Some reviews have focused on engineering challenges or the mechanics of dispersion and mixing (see Ghosal 2004; Locascio 2004; Stone, Stroock & Ajdari 2004). Many of these devices use liquid-phase electrokinetic phenomena to transport, separate and mix samples (see Harrison *et al.* 1992; Bruin 2000). Electrokinetics is a branch of electrohydrodynamics (EHD) that describes the coupling of ion transport, fluid flow and electric fields and is distinguished from EHD by the relevance of interface charge at solid–liquid interfaces (see Saville 1997). The fluid flow in this class of devices is often stable and strongly damped by viscous forces (with Reynolds numbers of order unity or smaller). However, heterogeneous

† Present address: Department of Mechanical and Aerospace Engineering, Arizona State University, Tempe, AZ 85287, USA. jonathan.posner@asu.edu

ionic conductivity fields in the presence of applied electric fields can, under certain conditions, generate an unstable flow field owing to electrokinetic instabilities (EKI). Conductivity gradients are prevalent in on-chip electrokinetic processes such as pre-concentration methods (e.g. field amplified sample stacking (see Bharadwaj & Santiago 2005) and isoelectric focusing (see Thormann, Mosher & Bier 1986)), multidimensional assays (see Herr *et al.* 2003), and systems with poorly specified sample chemistry. Electrokinetic instabilities can be leveraged for rapid mixing or can cause undesirable dispersion in sample injection, separation and stacking.

EHD flow instabilities in so-called 'leaky-dielectric' liquids (such as corn oil) with electrical conductivity gradients and applied electric fields have been observed since the 1960s (see Melcher & Taylor 1969). These instabilities are caused by a coupling of electric fields and ionic conductivity gradients that results in an electric body force (per unit volume) of the form $\rho_e \boldsymbol{E} = (\epsilon \boldsymbol{E} \cdot \nabla\sigma)\boldsymbol{E}$, where ϵ, $\boldsymbol{E}$ and σ are the local permittivity, electric field and ionic conductivity, respectively. In a seminal paper on EHD instability, Hoburg & Melcher (1976) showed that applying electric fields transverse to conductivity gradients in low-conductivity corn oil always results in unstable flows. Baygents & Baldessari (1998) performed a linear stability analysis of fields applied parallel to a linear conductivity gradient in high-conductivity electrolyte solutions. Their work was an effort to explain electrically driven distortion of scalar bands observed in isoelectric focusing experiments (see Rhodes, Snyder & Roberts 1989). Their analysis included the effects of ion diffusion and predicted conditionally unstable flow at relatively high electric Rayleigh numbers.

There has been revived interest in electrokinetic instabilities owing to recent anecdotal and qualitative descriptions of anomalous dispersion and unstable flow in electrokinetic pre-concentration methods used to increase the limit of detection of μTAS devices (see Shultz-Lockyear *et al.* 1999; Ramsey 2001; Dang *et al.* 2003). Oddy, Santiago & Mikkelsen (2001) observed electrokinetic instabilities in microchannel structures and made use of these instabilities for rapid continuous flow micromixing using a.c. fields. Lin *et al.* (2004) developed a modified ohmic model set of governing equations which is applicable to the study of electrokinetic instabilities with a symmetric binary electrolyte. In addition, Lin *et al.* presented limited experimental data, stability analyses, and detailed (two-dimensional and three-dimensional) numerical simulations for the temporal growth of disturbances that form at the interface of two liquid streams. They analysed the case of an electric field applied perpendicular to the conductivity gradient in a high-aspect-ratio microchannel. Storey *et al.* (2005) presented a depth-averaged version of the Lin *et al.* governing equations which compared well with the complete three-dimensional model for high-aspect-ratio channels. Chen *et al.* (2005) presented preliminary experiments and detailed stability analyses using depth-averaged linearized equations for the study of convective instability in the T-shaped intersection of two microchannel flow streams. In those experiments, Chen *et al.* visualized coherent wavelike disturbances that were convected downstream with the electro-osmotic flow. Chen *et al.* also showed that the flow became absolutely unstable at applied fields in excess of the critical applied field required for onset of instability. The symmetric binary electrolyte models of Lin *et al.*, Chen *et al.* and Storey *et al.* were extended to multiple ionic species by Oddy & Santiago (2005). The latter work shows that asymmetric ion mobilities can lead to significant reduction of the critical applied field required for instability. The destabilization of such systems is caused by the electromigration-driven transport of conductivity.

These EKI studies have focused on instabilities formed by applied fields perpendicular to a single conductivity interface. We have shown that sinuous

disturbances and coherent structures form on a layer of high-conductivity solution sandwiched between two low-conductivity streams in a cross-shaped microchannel (see Posner & Santiago 2004). This realistic cross-shape flow geometry is directly relevant to electrokinetic injection studies, sample pre-concentration processes that make use of conductivity gradients, and EK mixing schemes. Following the initial work on cross-shaped channels presented by Posner & Santiago, Shin, Kang & Cho (2005) used a.c. applied fields in an effort to further enhance mixing using EKI.

Previous EKI studies collectively provide a fundamental understanding of electrokinetic instabilities, identify key controlling parameters, present predictive simulations, and show preliminary experimental results. To date, there is no extensive experimental study of the critical applied field conditions required for instability (e.g. as a function of conductivity gradient and diffusion length scales), and there are no studies of realistic two- and three-dimensional flow geometries which occur in the intersections of isotropically etched microchannels. In the current work, we present a parametric experimental study of convective EKI in a cross-shaped microchannel using quantitative scalar imaging. We perform the experiments in an electrokinetic focusing flow configuration which is similar to the primary step of a pinched flow electrokinetic injection (or a three-inlet-channel mixing scheme), where the centre sample stream and sheath flows have mismatched ionic conductivities. As mentioned above, these conditions are relevant to on-chip electrokinetic practices with conductivity gradients such as sample injection for field-amplified sample stacking (see Ren & Li 2004; Bharadwaj & Santiago 2005), flow control and separations of streams with indeterminate sample chemistry, low-Reynolds-number micromixing (see Oddy *et al.* 2001), and flow at the intersection of multidimensional assays using heterogeneous buffer streams (see Herr *et al.* 2003). We explore variations of applied electric field and centre-to-sheath conductivity ratios that impose variations of the electric Rayleigh number across four orders of magnitude. Through interpretation of quantitative scalar imaging results, we show that the critical electric field required for instability depends on both the centre-to-sheath conductivity ratio and the applied field ratio that determines the width of the centre stream. We introduce scaling for the charge density (in the bulk fluid outside the electric double layer) as a function of the applied field, ionic conductivity ratio, and centre-stream width. We show that the flow becomes unstable at a critical electric Rayleigh number ($Ra_{e,\ell} = 205$) for a wide range of conductivity ratios (three orders of magnitude) and applied field ratios. Our formulation of the Rayleigh-number scaling is presented below.

The paper is structured as follows. In § 2, we describe the flow field and physical parameters in the system; in § 3, we derive a scaling relation for a modified local electric Rayleigh number and provide a control volume analysis for determining the local electric field and pressure gradients in the region of the chip where the instability develops; in § 4, we present the experimental set-up, electrolyte chemistry, and the methods used to record and reduce the scalar imaging data; in § 5, we introduce the instantaneous scalar images and present quantitative results reduced from the scalar images. We end § 5 with a comparison of trends and absolute values predicted by a simple model and the experimental data.

2. Description of the flow

In this work, we study instabilities that develop in the primary step of a pinched flow electrokinetic injection in a cross-shaped microchannel when the sample and sheath streams have different ionic conductivities. Figure 1 shows the cross-shaped

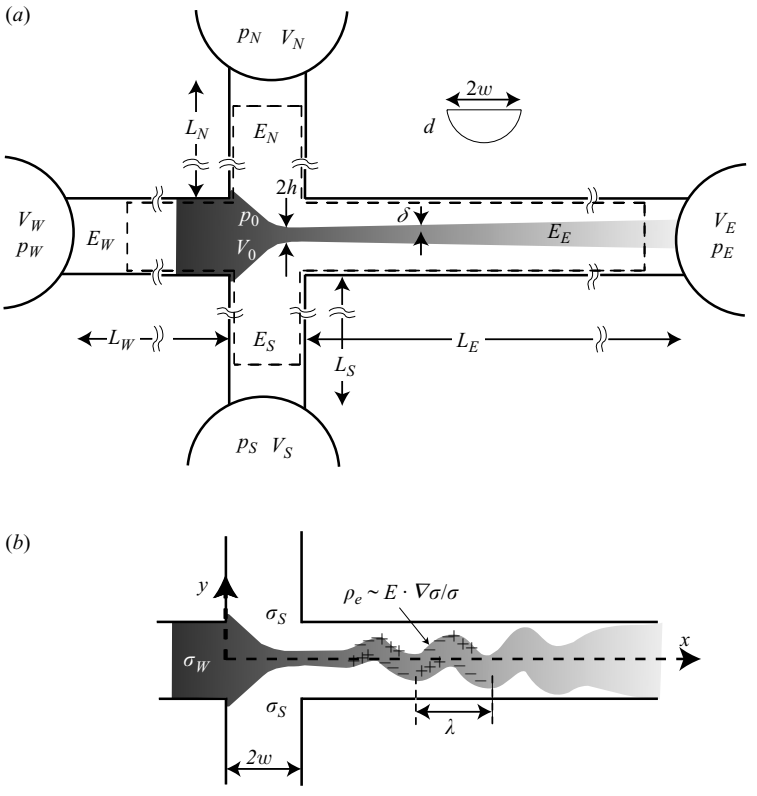

FIGURE 1. Schematic of (*a*) stable base state and (*b*) unstable flow in a cross-shaped microchannel. The channels have the characteristic D-shape cross-sections of isotropic etching with half-width w, depth d and lengths L_n. Buffered aqueous solutions flow towards the channel intersection from the north (top), south (bottom), and west (left) wells and flow away from the intersection along the x-axis (streamwise direction) towards the east (right) well. The sheath streams from the north and south wells have an ionic conductivity σ_S and the sample stream from the west well has a conductivity σ_W. The sheath streams flow symmetrically from the north and south wells forming two conductivity interfaces and confining the centre sample stream to a minimum thickness of half-width, h. The ions and tracer dye in the centre sample stream diffuse into the sheath streams with a diffusive penetration length δ. Applied electric fields couple with conductivity gradients to generate charge density ρ_e in the bulk fluid. These net charge regions result in electric body forces that can destabilize the flow. For the condition shown here, sinuous perturbations with a nominal wavelength λ grow and convect downstream.

microchannel and base state flow. This schematic shows the region of interest that is approximately 600 μm wide and 150 μm in the vertical dimension. This region of flow instability formation and development is a small fraction of the active chip area. The wells are shown at the ends of abbreviated channel lengths. The channels have the characteristic D-shape cross-sections of isotropic etching with a half-width w, depth d, and lengths L_n. Buffered aqueous solutions flow toward the channel intersection from the north (top), south (bottom) and west (left) wells, and flow away from the intersection along the x-axis (streamwise direction) towards the east (right) well. The sheath streams flow symmetrically from the north and south wells confining the centre sample stream in the channel intersection into a triangle-shaped 'head'. Downstream of the head, the centre stream is focused to a narrow half-width of h. We will call

this point of minimum width of the centre stream the 'throat'. In all cases, the centre stream is dyed with an electrically neutral fluorescent tracer dye. The sheath streams from the north and south wells both have an ionic conductivity σ_S, and the sample stream from the west well has a conductivity σ_W. We define the conductivity ratio as $\gamma = \sigma_W/\sigma_S$. In the east channel, the centre stream is sandwiched between sheath streams forming a double conductivity interface. The ions and tracer dye molecules in the centre stream diffuse into the sheath streams with a diffusive penetration length that scales as $\delta = \sqrt{D_{eff}\, x/U}$, where D_{eff} is the effective diffusivity, x is the downstream location, and U is the streamwise advection velocity.

In general, the velocity in each channel depends on the local electric field E_n, the electro-osmotic mobility (which depends on the ionic concentration and pH), and both imposed and internally-generated pressure gradients. We apply potentials V_n at end-channel wells and impose no pressure gradient so that $p_E = p_S = p_W = p_N$. In § 3.3, we develop a control volume model to describe the electric field and internally-generated pressure gradient in each channel as a function of the applied potentials, V_n, and electrolyte conductivities. Symmetry of the sheath flows about the x-axis is maintained by the applied potentials in the north and south wells. The width of the centre stream is controlled by the ratio of the west (sample) well to the north and south (sheath) well potentials.

As we shall discuss, electrokinetic flows become unstable when the distortion of the conductivity interfaces due to internally-generated electroviscous velocities occurs more rapidly than the dispersion of this interface due to molecular diffusion. Figure 1(*b*) shows an unstable electrokinetic flow. Applied electric fields couple with conductivity gradients to generate charge density ρ_e in the bulk flow (outside the thin electric double layer). For the condition shown here, sinuous perturbations, with a nominal wavelength λ, grow and convect downstream.

3. Theory

In this section, we first develop scaling relations for a electric Rayleigh number that accounts for the local scaling of charge density as a function of the maximum conductivity gradients. We then apply a control volume approach to solve for the electric field and internally generated pressure gradient in the east channel as a function of the directly specified experimental parameters.

3.1. *Scaling analysis*

The governing equations for EKI in a symmetric binary electrolyte are adopted from the modified ohmic model of Lin *et al.* (2004). Here, we briefly describe the derivation of the governing set of equations. We start with the conservation equation for mass (3.1), the conservation of momentum with an electric body force (3.2), Poisson's equation (3.5), and two convective diffusion equations for a dilute two-species electrolyte. Using the definitions of the ionic conductivity and free charge density (equations (3.6*a*) and (3.6*b*), respectively) the convective diffusion equations are recast into conservation equations for ionic conductivity σ and free charge density ρ_e (see equations 8 and 9 in Lin *et al.*). Scaling of these conservation equations results in a smallness parameter $\Delta C_0/C_0$, where C_0 is the total concentration of the ions and ΔC_0 is the difference of concentration of anion and cation. As we shall discuss in detail below, this concentration difference is proportional to the internal field generated by net charge density. For flows where the internal field is generated by the interaction of an applied electric field and a conductivity gradient, we show that

ΔC_0 scales as $\epsilon E_0(\gamma - 1)/\mathrm{F}\delta\gamma$, where E_0 is the local electric field, γ is the ionic conductivity ratio, and δ is the length scale over which changes in conductivity occur. Microscale electrokinetic flows often have small δ (approximately 1 to 10 μm in the current flow), E_0 of the order of $100\,\mathrm{V\,cm^{-1}}$, and C_0 of 1 mM or larger. For the flows of interest here, $(\gamma - 1)/\gamma$ is of order unity, $\epsilon E_0(\gamma - 1)/\mathrm{F}\delta\gamma$ is of the order of 10^{-5} and $\Delta C_0/C_0$ is of the order of 10^{-6}. This suggests we can invoke the electroneutrality condition ($C_+ \approx C_-$) in predictions of the species concentration field development.

In the limit of small $\Delta C_0/C_0$, we can write two simplified formulations for conservation of conductivity field (3.3) and the conservation of electromigration current (3.4). The details of these derivations can be found in Lin *et al.* (2004) and Chen *et al.* (2005). The non-dimensional modified ohmic model governing equations are therefore given as,

$$\nabla \cdot \boldsymbol{v} = 0, \tag{3.1}$$

$$Re\left(\frac{\partial \boldsymbol{v}}{\partial t} + \boldsymbol{v} \cdot \nabla \boldsymbol{v}\right) = -\nabla p + \nabla^2 \boldsymbol{v} - \rho_e \boldsymbol{E}, \tag{3.2}$$

$$\frac{\partial \sigma}{\partial t} + \boldsymbol{v} \cdot \nabla \sigma = \frac{1}{Ra_e} \nabla^2 \sigma, \tag{3.3}$$

$$\nabla \cdot (\sigma \boldsymbol{E}) = 0, \tag{3.4}$$

$$\nabla \cdot (\epsilon \boldsymbol{E}) = \rho_e. \tag{3.5}$$

The non-dimensionalized two-ion electrical conductivity and charge density are, respectively, defined as,

$$\sigma \equiv \frac{\mathrm{F}^2(\Lambda_+ C_+ z_+^2 + \Lambda_- C_- z_-^2)}{\sigma_0}, \tag{3.6a}$$

$$\rho_e \equiv \frac{\mathrm{F}(C_+ z_+ - C_- z_-)}{\epsilon E_0 / w}, \tag{3.6b}$$

where F is Faraday's constant, z is the valance number, and Λ is mobility. The relevant non-dimensional parameters are the Reynolds number,

$$Re \equiv \frac{\rho_0 U_{ev} d}{\mu}, \tag{3.7}$$

the electric Rayleigh number

$$Ra_e \equiv \frac{U_{ev} w}{D_{eff}}, \tag{3.8}$$

and the ratio of electroviscous velocity, U_{ev} to electro-osmotic velocity,

$$R_v \equiv \frac{E_0 d}{\zeta}. \tag{3.9}$$

Here, ρ_0 is the electrolyte solution density, E_0 is the local electric field, w is the channel half-width, d is the channel depth, ζ is the zeta-potential, and D_{eff} is the effective molecular diffusion coefficient. For now, we have considered a straightforward scaling of the momentum equation (3.2) and conductivity convective-diffusion equation (3.3) in terms of the channel depth d and the channel half-width w, respectively. In the next section, we will present an alternative scaling for a local value of electric Rayleigh number based, in part, on a diffusion-layer length scale. The electro-osmotic wall velocity is characterized in terms of the zeta-potential ζ and the local electric field E_0 (see Hunter 1981). The velocity used in the Reynolds- and Rayleigh-number

scaling is the electroviscous velocity derived from the balance of viscous and electrical body forces in the momentum equation (3.2), given as,

$$U_{ev} = \frac{\rho_e E_0}{\mu/d^2}. \tag{3.10}$$

In this work, *Re* is of the order of 0.1. The Rayleigh number is the ratio of the electroviscous and diffusive velocities. The charge density term ρ_e in (3.10) forms in the bulk regions of the flow containing conductivity gradients, and couples with the applied field to generate electrical body forces in the bulk liquid. In a seminal paper on electrohydrodynamic instabilities of so-called 'leaky-dielectrics', Hoburg & Melcher (1976) showed that the accumulation of free charge ρ_e in regions of conductivity gradients and collinear applied fields is described by the conservation of the electromigration current (3.4) and Gauss's law (3.5). This coupling can be quantified as

$$\rho_e = -\epsilon \boldsymbol{E} \cdot \frac{\nabla \sigma}{\sigma}. \tag{3.11}$$

We now briefly summarize formulations of electric Rayleigh numbers reported in the literature and their applicability to electrokinetic instabilities. Table 1 shows four formulations of critical electric Rayleigh number for studies of electrohydrodynamic instabilities with interfaces between miscible liquids where ion diffusion is significant. We compare these definitions to the current formulation of a local Rayleigh number (see § 3.2). In the third column, we give a ratio of the local electric Rayleigh number presented here (see equation (3.19)) to the Rayleigh number defined in each reference. The last column lists the critical Rayleigh number corresponding to the onset of instability extracted from each reference. Note that these critical values are generated from various models (as discussed in § 1) and depend on conductivity ratio, γ and model type (i.e. two- or three-dimensional or depth-averaged equations).

The main difference among Rayleigh numbers in the table is the scaling of electroviscous velocity, U_{ev}. The formulation of electroviscous velocity depends on the scaling of charge density and the length scale that characterizes viscous stresses. The simplest formulation is adopted by Hoburg & Melcher and Lin *et al.* where charge density scales such that the internally generated electric field is of the order of the applied field, given as $\rho_e = \epsilon E/w$. Baygents & Baldessari scaled charge density with a linear conductivity gradient as $\epsilon E \Delta\sigma/(\sigma w)$, where w is both the width of the channel and the length over which conductivity gradients occur. Lin *et al.* showed that the critical electric Rayleigh number required for onset of electrokinetic instability in microchannels varied from 10^3 to 10^5, depending on the value of the conductivity ratio. Lin *et al.* also showed that, in shallow channels, the shallow depth dimension dominates viscous stresses and significantly stabilizes the flow. Storey *et al.* and Oddy & Santiago considered these stabilizing effects by scaling the viscous stresses with the thin channel depth, d. One limitation of the Rayleigh-number formulations adopted by Lin *et al.*, Storey *et al.* and Oddy & Santiago is that, unlike that of Baygents & Baldessari, it does not account for the dependence of charge density on the magnitudes of conductivity gradients.

Chen *et al.* used arguments similar to those presented by Baygents & Baldessari, but also considered nonlinear scaling of the charge density with a formulation for perturbed electric fields. Another contribution by Chen *et al.* was a scaling of the charge density with a diffusion thickness, δ.

In the current work, our goal is to derive a scaling for charge density and electroviscous velocity that accounts for the maximum local values of conductivity gradients that occur in a cross-shaped channel. This flow is distinct from previous

work, at least in that there are two conductivity interfaces and an additional length scale, the half-width of the centre stream, h. This scaling for an electric Rayleigh number based on local conductivity gradients is presented in the next section.

3.2. *Local electric Rayleigh number scaling*

In this section, we present a derivation of the relevant electric Rayleigh number that describes the onset of EKI. In an effort to generalize the formulation to systems with two- and three-dimensional conductivity gradients (as found in our flow), we formulate Ra_e in terms of a local conductivity gradient. First, we non-dimensionalize the conductivity convective-diffusion equation (3.3) and charge density equation (3.11) with the following scales: $\boldsymbol{E}^* = \boldsymbol{E}/E_a$, $\sigma^* = (\sigma - \sigma_L)/\Delta\sigma$, and $\nabla^* = \nabla\delta$, where $\Delta\sigma = \sigma_H - \sigma_L$ and the asterisk denotes a dimensionless variable with order unity. Next, we define a local Rayleigh number for the flow, based on a local value of diffusion thickness δ as

$$Ra_{e,\ell} \equiv \frac{U_{ev}\delta}{D_{eff}}. \tag{3.12}$$

The non-dimensional charge density is then written as

$$\rho_e = -\frac{\epsilon E_a}{\delta}\frac{\Delta\sigma}{\sigma_H}\frac{\boldsymbol{E}^* \cdot \nabla^*\sigma^*}{\sigma^*}. \tag{3.13}$$

Since we are interested in a Rayleigh formulation that characterizes the onset of instability, we scale the conductivity gradient with the local value of the conductivity field diffusion thickness, δ. This scaling of the convective-diffusion equation is distinct from previous formulations which use the channel height w (see Hoburg & Melcher 1976; Baygents & Baldessari 1998; Lin *et al.* 2004; Oddy & Santiago 2005; Storey *et al.* 2005). In comparison, Chen *et al.* scaled the charge density with the diffusion length scale δ and scaled the advection and diffusion of conductivity gradients with the channel half-height w (see table 1). This was appropriate to their flows as the normalized diffusion thickness $\delta/2w$ was of order unity (which was also the case for Baygents & Baldessari 1998). In our flow, the normalized diffusion thickness $\delta/2w$ can be of order of 0.1 or less, and so we distinguish between the maximum characteristic length scale over which conductivity gradients can occur, w, and the actual length scale of these gradients, δ.

In the nearly parallel flow of the east channel, we can estimate diffusion thickness, using a simple one-dimensional formulation for diffusion along the spanwise direction. The time scale for this diffusion is the streamwise advective time scale x/u_{eo}, so that

$$\delta \sim \sqrt{\frac{x D_{eff}}{u_{eo}}}, \tag{3.14}$$

where x is the streamwise location (from the left-most edge of the channel intersection) and u_{eo} is approximately the cross-sectional-area-averaged electro-osmotic velocity in the east channel. The electro-osmotic velocity is a function of the zeta-potential and applied field through the Helmholtz–Smoluchowski equation,

$$u_{eo} = -\frac{\epsilon\zeta E_0}{\mu}, \tag{3.15}$$

where E_0 the local field in the east channel.

Next, we explore the effects of the length scales h, w and δ on the maximum conductivity gradient by analysing the quasi-one-dimensional spanwise diffusion of the centre stream in the domain bounded by $y = \pm w$. In the stable nearly-parallel flow, we approximate the initial three-dimensional conductivity distribution of the centre stream (at the throat) as a one-dimensional diffuse top-hat distribution in the spanwise

Ra_e formulation	Reference	$Ra_{e,\ell}/Ra_e$	$Ra_{e,c}$
$\frac{4\epsilon E^2 w^2}{D\mu}\frac{\Delta\sigma}{\sigma_0}$	Baygents & Baldessari	$\frac{d^2}{4w^2}\frac{1}{\gamma}\nabla^*\sigma^*\vert_{max}$†	1.4×10^4
$\frac{\epsilon E^2 w d^2}{D\mu\delta}\left(\frac{\gamma-1}{\gamma+1}\right)^2$	Chen *et al.*	$\frac{\delta}{w}\frac{(\gamma+1)^2}{\gamma(\gamma-1)}\nabla^*\sigma^*\vert_{max}$	10
$\frac{\epsilon E^2 w^2}{D\mu}$	Lin *et al.*[a]	$\frac{d^2}{w^2}\frac{\gamma-1}{\gamma}\nabla^*\sigma^*\vert_{max}$	1100‡,10^4–10^5‖, 1200¶
$\frac{\epsilon E^2 d^2}{D\mu}$	Storey *et al.*[b]	$\frac{\gamma-1}{\gamma}\nabla^*\sigma^*\vert_{max}$	400
$\frac{\epsilon E^2 d^2}{D\mu}\frac{\gamma-1}{\gamma}\nabla^*\sigma^*\vert_{max}$	Current	1	205

† We have translated the linear conductivity gradient $\Delta\sigma/\sigma_0$ to $\gamma-1$.
‡ Three-dimensional calculation, from Storey *et al.* (2005).
‖ Two-dimensional calculation, $Ra_{e,c}$ function of conductivity ratio varied from 10 to 1.5, from Lin *et al.* (2004).
¶ Three-dimensional calculation conductivity ratio of 10 from Lin *et al.* (2004).

TABLE 1. Definitions of electric Rayleigh number used by various authors. The third column is the ratio of the modified Rayleigh number presented in equation 3.19 and cited definition. The final column is the critical Rayleigh number reported for each definition.[a] also used by Storey *et al.* (2005),[b] also used by Oddy & Santiago (2005).

(y) direction. The conductivity distribution develops via spanwise diffusion over a time x/u_{eo} where x is the downstream location. The one-dimensional normalized spanwise diffusion of a top hat with an initial half-width h in a bounded domain can be solved exactly using a Green's function approach (see Crank 1975) as

$$\sigma^*(y;x) = \frac{1}{2}\left[\mathrm{erf}\left(\frac{h+y}{2\delta}\right)+\mathrm{erf}\left(\frac{h-y}{2\delta}\right)+\sum_{n=2}^{\infty}\left[\mathrm{erf}\left(\frac{h+y-nw}{2\delta}\right)+\mathrm{erf}\left(\frac{h+y+nw}{2\delta}\right)+\mathrm{erf}\left(\frac{h-y+nw}{2\delta}\right)+\mathrm{erf}\left(\frac{h-y-nw}{2\delta}\right)\right]\right], \tag{3.16}$$

where the first two terms account for the diffuse top-hat profile and the sum term accounts for reflections from the walls at $y=\pm w$. The diffusion thickness increases with downstream location, as described by equation (3.14). If we account for only the first set of reflections ($n=2$), approximate the location of the maximum conductivity gradient as $y=\pm h$, neglect terms of the order $\exp(-(w/\delta)^2)$ and smaller, and normalize, we obtain an approximate solution for the normalized maximum conductivity gradient,

$$\nabla^*\sigma^*\Big|_{max} \approx \frac{\mathrm{d}\sigma^*}{\mathrm{d}(y/\delta)}\Big|_{max} \approx 1-\exp\left(-\left(\frac{h}{\delta}\right)^2\right)-\exp\left(-\left(\frac{w-h}{\delta}\right)^2\right). \tag{3.17}$$

Details of this derivation are given in the Appendix. The analysis shows that the magnitude of the maximum conductivity gradient in the channel scales as exponential functions of the length ratios h/δ and $(w-h)/\delta$. When the centre or sheath stream widths are of the order of the spanwise diffusion thickness, the conductivity gradient

is rapidly homogenized by diffusion. That is, the maximum conductivity gradient is reduced for both $h/\delta \leqslant 1$ (small centre stream width) and $(w-h)/\delta \leqslant 1$ (small sheath stream width). The non-dimensional charge density equation is

$$\rho_e = -\frac{\epsilon E_a}{\delta}\frac{\Delta\sigma}{\sigma_H}\boldsymbol{E}^* \cdot \frac{\nabla^*\sigma^*}{\sigma^*} = -\frac{\epsilon E_a}{\delta}\frac{\gamma-1}{\gamma}\frac{\boldsymbol{E}^* \cdot \nabla^*\sigma^*}{\sigma^*} \tag{3.18a}$$

and scales as

$$\rho_e \sim -\frac{\epsilon E_a}{\delta}\frac{\gamma-1}{\gamma}\nabla^*\sigma^*\Big|_{max}, \tag{3.18b}$$

where the non-dimensional quantities are of order unity and $\gamma = \sigma_H/\sigma_L$. Combining equations (3.10), (3.12) and (3.18*b*), the modified local electric Rayleigh number becomes

$$Ra_{e,\ell} \equiv \frac{\epsilon E_a^2 d^2}{D_{eff}\mu}\frac{\gamma-1}{\gamma}\nabla^*\sigma^*\Big|_{max} \approx \frac{\epsilon E_a^2 d^2}{D_{eff}\mu}\frac{\gamma-1}{\gamma}\frac{\mathrm{d}\sigma^*}{\mathrm{d}(y/\delta)}\Big|_{max}, \tag{3.19}$$

where $\nabla^*\sigma^*|_{max}$ is defined by equation (3.17). This definition of local modified electric Rayleigh number accounts for scaling of the charge density as a function of the maximum conductivity gradients in our flow. The maximum conductivity gradients are governed by the imposed conductivity ratio γ, the centre stream width h, and the local diffusion thickness δ. Note that we approximate the length scale that characterizes viscous stresses with the depth of the channel d (the width of our channels is 2.5 times larger than their depth). We also approximate the length scale that characterizes conductivity gradients with the diffusion thickness δ. This scaling results in a local Rayleigh formulation that is only dependent on the diffusion thickness δ and the channel half-width w through the local value of $\nabla^*\sigma^*|_{max}$. In § 5.8 we will show that this local electric Rayleigh number formulation (3.19) well describes trends of instability onset observed in our experiments.

3.3. *Control volume analysis*

In this section, we present a control volume analysis conserving fluid flow, electric flux, and electric current. The analysis provides us with an estimate of the internally generated pressure gradients in the system as a function of the applied potentials and conductivity ratio. We are interested in the average electric field and pressure gradient in the east channel where the instability grows and develops. We solve for the east channel, pressure and potential gradients as a function of the independent experimental parameters, namely the conductivity ratio γ, electric field ratio β, and the nominal applied field E_a, as defined below. The control surface of interest is shown in figure 1(*a*) as a dashed line. This surface is taken as bounding the bulk liquid in the channel, but excludes the electric double layer near the walls. Wall shear stress at such a 'slip surface' is balanced strictly by pressure gradients along the channel (see Santiago 2001) and, to a lesser degree, body forces in the bulk.

Although the electric field, ionic conductivity, and zeta-potential near the intersection are typically a dynamic function of the flow field, we will for now assume these are uniform within each channel, with a discontinuity at the channel intersection. This assumption is justified considering that the intersection and the region of the east channel which contain strong conductivity gradients make up a small portion of the total channel system. Note that, even in the stable base state condition, the solutions are well mixed by diffusion and are homogeneous within about 20 channel half-widths from the intersection, while our east channel length is 3200 channel half-widths long.

We begin the control volume analysis by satisfying conservation of the electromigration current and volume flux. The integral forms of equations (3.1) and (3.4) are

$$Q = \oint_A \boldsymbol{U} \cdot \mathrm{d}\boldsymbol{A} = 0, \tag{3.20}$$

$$i = \oint_A \sigma \boldsymbol{E} \cdot \mathrm{d}\boldsymbol{A} = 0, \tag{3.21}$$

where i and Q are the net current and volume fluxes through the control surface. Equations (3.20) and (3.21) assume negligible diffusive and advective current fluxes and no net accumulation of charge, consistent with the ohmic model formulation. The slip surface can be assumed to be electrically insulated and impenetrable (see Santiago 2001), so that $\boldsymbol{U} \cdot \mathrm{d}\boldsymbol{n}$, $\boldsymbol{E} \cdot \mathrm{d}\boldsymbol{n} = 0$, where $\boldsymbol{n}$ is the wall normal. The flow rate in each channel is a function of the local field and pressure gradient, given as

$$Q_n = -\int_A \left(\frac{\epsilon \zeta E_n}{\mu} + \frac{1}{fRe} \frac{2D_h^2}{\mu} \frac{\partial p}{\partial x}_n \right) \mathrm{d}A, \tag{3.22}$$

where D_h is the hydraulic diameter, f is the appropriate Fanning-type friction factor, and Re is the Reynolds number, based upon the area-averaged velocity and the hydraulic diameter. The product fRe is tabulated for a wide range of geometries in Shah & London (1978). For the D-shaped microchannels used here, Shah & London give a value of 15.767 for fRe. We define the nominal pressure gradient and electric fields in each channel as,

$$E_n \equiv \frac{V_0 - V_n}{L_n}, \tag{3.23}$$

$$\frac{\partial p}{\partial x}_n \equiv \frac{p_0 - p_n}{L_n}, \tag{3.24}$$

where the subscript n may denote the east (E), north (N), west (W) and south (S) wells, and (0) denotes the channel intersection. Consistent with the symmetry of our flow about the x-axis, we set $Q_\mathrm{N} = Q_\mathrm{S}$. The conductivity in the east channel is approximated as the volume flux average of the west, north and south channels, so that $\sigma_\mathrm{E}/\sigma_\mathrm{S} = (\gamma Q_\mathrm{W} + 2Q_\mathrm{S})/Q_\mathrm{E}$. The local volume-averaged ionic conductivity and the electro-osmotic slip velocity are coupled through a dependence of the zeta-potential on the local ionic species concentration. The electro-osmotic mobility of glass is generally considered to be a function of the electrolyte ion concentration and pH (see Hunter 1981; Kirby & Hasselbrink 2004). In our experiments, we have uniform pH and the dependence of the potential is modelled by a power-law equation of the form

$$\frac{\zeta}{\zeta_0} = \left(\frac{\sigma}{\sigma_0} \right)^{-m}, \tag{3.25}$$

where m is a power law coefficient, and the subscript denotes a reference condition. Values for varying from 0.15 to 0.5 have been suggested by various authors (see Hunter 1981; Scales *et al.* 1992; Szymczyk *et al.* 1999). We will assume here a value of 0.3 which is consistent with results of both Sadr *et al.* (2004) and Yao *et al.* (2003). The zeta-potential of the north and south channels are equal, $\zeta_N = \zeta_S$ and the respective zeta-potentials in the west and east channels are a function of gamma $\zeta_W = \zeta_S \gamma^{-m}$ and $\zeta_E = \zeta_S (\sigma_E/\sigma_S)^{-m}$.

Equations (3.20)–(3.24) determine the pressure gradient and electric field in the east channel as a function the conductivity ratio γ, the nominally applied field E_a, and

electric field ratio β. The quantities E_a, β and γ are defined as

$$E_a \equiv \frac{V_S - V_E}{L_E + L_S}, \tag{3.26}$$

$$\beta \equiv \frac{(V_W - V_E)/(L_W + L_E)}{E_a}, \tag{3.27}$$

$$\gamma \equiv \frac{\sigma_W}{\sigma_S}. \tag{3.28}$$

The nominal applied field for the flow field is defined as the potential applied between the south and east channel reservoirs divided by the appropriate channel lengths. This definition is useful as the characteristic field is then a function of directly specified experimental parameters. The electric field ratio β is a ratio of the west and south nominal fields and controls the centre-to-sheath flow-rate ratio and the centre stream half-width h, as will be shown in § 4.3.

An explicit analytical expression for the pressures and electrical potentials in the system is difficult to obtain. The roots that satisfy both equations (3.20) and (3.21) were obtained using an iterative Newton–Raphson method to determine the pressure and potential at the intersection. The pressure p_0 and electrical potential V_0 at the intersection were then substituted into equations (3.24) and (3.26) to determine the pressure gradient $\partial p/\partial x_E$ and electric field in the east channel E_E. We impose no external pressure differences (i.e, $p_E = p_W = p_S = p_N$), but electrokinetic flows with heterogeneous electrolytes or zeta-potentials may generate internal pressure gradients (see Burgi & Chien 1991; Devasenathipathy 2003; Ren & Li 2004; Bharadwaj & Santiago 2005).

Figure 2 shows a contour map of the internally generated nominal pressure gradient in the east channel as a function of the applied field E_a and the conductivity ratio $\gamma \geqslant 1$, for the $\beta = 1$ case. The (negative) pressure gradients are favourable and generate flow in the direction of electro-osmotic flow. For γ values greater than unity, the pressure gradient increases linearly with the applied field E_a with a slope weakly dependent on γ. For a given electric field, the pressure gradient magnitude initially increases exponentially with γ and then saturates to a maximum value at $\gamma \approx 20$. For further increases in γ, the pressure gradient magnitude slowly decreases. In all cases of interest, the largest pressure gradients generate volume fluxes that are always less than 4% of the total volume flux.

We found power law (and linear) curve fits to the electric field solutions using a non-linear regression procedure. The electric field in the east channel as a function of the nominally applied field E_a, the field ratio β and the conductivity ratio γ, can be expressed as

$$E_E(E_a, \beta, \gamma) = a(\beta) E_a \gamma^{n(\beta)}, \tag{3.29a}$$

$$a(\beta) = 0.30\beta + 0.46, \tag{3.29b}$$

$$n(\beta) = 0.39\beta^{6.6}, \tag{3.29c}$$

The field in the east channel is a linear function of the nominally applied field E_a and a power-law function of the west-to-south field ratio β and the conductivity ratio γ. We plot our experimental results as a function of the nominally applied field E_a (which is a known function of the directly controlled experimental electrical potential V_S given in (3.23)). Equations (3.29*a*)–(3.29*c*) can be used to determine approximately the local value of the electric field in the east channel, where the instability develops.

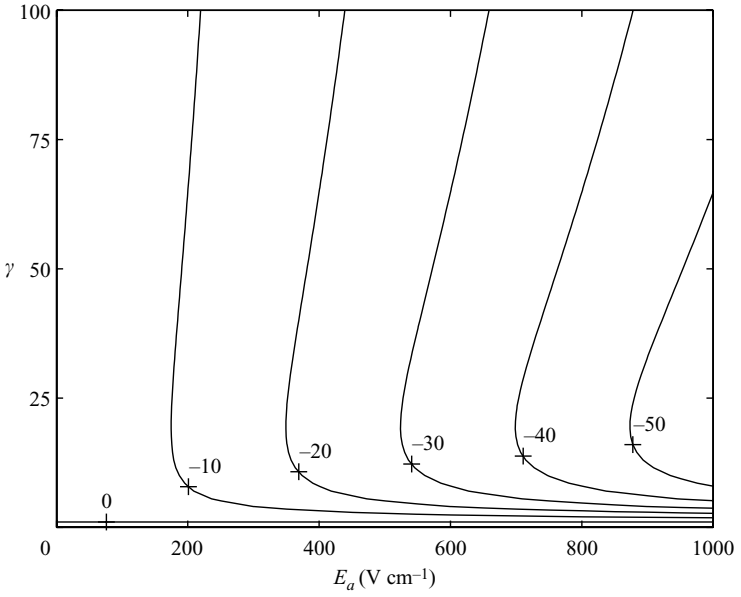

FIGURE 2. Contour map of internally generated pressure gradients (atm m^{-1}) in the east channel as a function of the applied field, E_a, and centre-to-sheath conductivity ratio γ and field ratio $\beta = 1$. The (negative) pressure gradients are favourable and generate flow in the direction of electro-osmotic flow. In all cases of interest here, the largest pressure gradients generate volume fluxes that are less than 4% of the total volume flux.

4. Exprimental methodology

In this section, we describe our epifluorescence microscopy imaging system, electronics, electrolyte chemistry, and the methods used to record and reduce the scalar imaging data.

4.1. *Imaging and electronics*

We obtained instantaneous concentration fields of rhodamine B using epifluorescence microscopy and CCD camera imaging. Figure 3 shows the experimental set-up. Experiments were performed in cross-shaped, isotropically etched (D-shaped) glass channels 50 μm wide and 20 μm deep (Micralyne, Alberta, Canada). The channel lengths are 85, 5, 4 and 5 mm for the north, east, south and west channels, respectively. Electrical potentials were applied using platinum electrodes to electrolyte solutions in 50 μL channel reservoirs fabricated from HPLC fittings (Upchurch, Oak Harbor, WA, USA). The potentials were applied and synchronized to CCD image acquisitions using a high-voltage sequencer (LabSmith, Livermore, CA, USA). The high-voltage sequencer is limited to 3 kV potentials. A four-channel high-voltage power supply (Micralyne, Alberta, Canada) was used for experiments requiring higher applied potentials. A microscope (Nikon, Japan) with a 20×, NA = 0.45 ELWD objective (Nikon, Japan), mercury bulb illumination, and epifluorescence filter cube (excitation at 540 nm, emission at 625 nm; Chroma, Rockingham, VT, USA) were used to image the flow. Images were recorded on a Peltier-cooled, 16-bit CCD camera with on-chip gain (Photometrics, Tucson, AZ, USA). The exposure time of each image was controlled by a liquid-crystal video-rate shutter (Displaytech, Longmont, CO, USA).

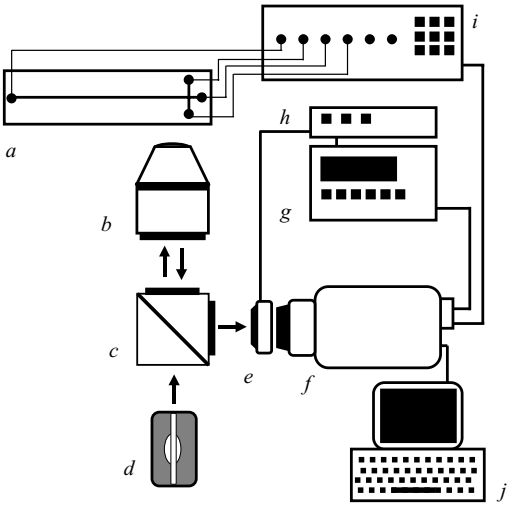

FIGURE 3. Experimental set-up of epifluorescence microscopy for imaging fluorescent dye concentration in electrokinetic flows. System components are the following: *a*, glass microchip; *b*, objective; *c*, epifluorescence filter cube; *d*, mercury bulb; *e*, liquid crystal video shutter; *f*, charged couple device camera; *g*, digital delay; *h*, liquid-crystal driver; *i*, high-voltage sequencer; and *j*, computer.

We correct each image of scalar concentration for systematic errors with the equation

$$C_j(x, y) = \frac{I_j(x, y)_{raw} - \overline{I(x, y)_{dark}}}{\overline{I(x, y)_{flat}} - \overline{I(x, y)_{dark}}}, \tag{4.1}$$

where,

$$\overline{I(x, y)} = \frac{\sum_{j=1}^{n} I_j(x, y)}{n - 1}. \tag{4.2}$$

The instantaneous image index is j and the subscripts *raw*, *flat* and dark denote the raw, flat-field and dark-field images, respectively. The flat-field images are recorded with the channels filled with a uniform concentration of dye and correct for illumination non-uniformity and detector response. The dark-field images are recorded with the channels filled with buffer. The dark-field images correct for external light scattered off channel walls and not chromatically filtered fluorescence of wall adsorbed dye, and sensor dark-noise. We record two hundred dark and flat-field images before each experiment.

Depth averaging along the optical axis (z-direction) is an artefact of fluorescence imaging. Contributions to the measured fluorescence are made across the imaging depth of field. Although depth-of-field definitions for microscopic imaging vary, Inoué & Spring (1997) define the geometric and diffraction contributions to the depth of field as

$$\delta z = \frac{n\lambda_c}{\mathrm{NA}} + \frac{ne}{M\mathrm{NA}}, \tag{4.3}$$

where n is the index of refraction of the immersion medium, λ_c is the collection wavelength, NA is the objective numerical aperture, M is the objective magnification, and e is the smallest resolvable distance of the detector. Using this definition, the depth of field for a 20×, NA = 0.45 objective is $\delta z = 4.4$ μm. This depth cannot be strictly interpreted as the region over which the fluorescence is measured, but it suggests that

Symbol	Description	Value
ϵ_0	Universal permittivity	8.85×10^{-12} C V^{-1} m^{-1}
ϵ_r	Relative permittivity	78.3
μ	Dynamic viscosity	1.0×10^{-3} kg m^{-1} s^{-1}
ρ	Density of water	1.0×10^{3} kg m^{-3}
D_{eff}	Effective diffusivity (KCl)	2.0×10^{-9} m^2 s^{-1}
Λ	Mobility	8.2×10^{-13} mol s kg^{-1}
F	Faraday's constant	9.65×10^{4} C mol^{-1}
ζ_0	Reference zeta-potential	-1.0×10^{-2} V
w	Channel half-width	2.5×10^{-5} m
d	Channel depth	2.0×10^{-5} m

TABLE 2. Electrolyte solution and microchip experimental parameters and fundamental scales. The effective diffusivity of potassium chloride (KCl) is calculated using equations from Probstein (1994) and tabulated values from Lide (1997).

the recorded images do not strictly represent a thin slice of the 20 μm deep channel. Collected image intensities are therefore a superposition of dye emission from an approximately in-focus, 4 μm thick region and fluorescence emission from dye above and below the focal plane. In all experiments, we set the focal plane at about 10 μm from the channel top wall. Note that confocal microscopy cannot be used to obtain depth-resolved scalar measurements in these experiments owing to the rapid dynamics of the instability.

4.2. *Electrolyte solutions*

The stock aqueous buffered solutions consisted of 10 mM HEPES hemisodium salt (Sigma Aldrich, St Louis, MO, USA) in filtered deionized water (Fisher Scientific W2-20, Fairlawn, NJ, USA). The pH of the buffered solutions were 7.5 as measured using a pH meter (Corning, Corning, NY, USA). Potassium chloride (Sigma Aldrich, St Louis, MO, USA) was added to the stock solutions to obtain desired conductivities. We filtered the electrolyte solutions prior to the experiments with 200 nm syringe filters (Nalgene Labware, Rochester, NY, USA). The conductivity of the west well solution σ_W was measured as 40 mS cm^{-1} and 0.40 mS cm^{-1}, respectively for the $\gamma > 1$ and $\gamma < 1$ experiments using a conductivity meter (CON Oakton Instruments, Vernon, IL, USA). The north and south well solution conductivities σ_S were in all cases identical and varied from 0.4 mS cm^{-1} to 40 mS cm^{-1}. The conductivity ratio γ was varied from 0.01 to 100. Other properties of the working liquids are shown in table 2.

To visualize fluid motion, 10 μM of electrically neutral, rhodamine B dye (Acros Organics, Geel, Belgium) was added to the west well solution. To improve the clarity of the visualizations shown in figure 4 (and for these visualizations alone), we used 10 mM, high molecular weight (70 kDa), dextran conjugated rhodamine B dye (Molecular Probes, Eugene, OR, USA).

4.3. *Experimental conditions*

In our parametric investigation, we recorded data for fifteen values of γ, eleven values of β, and applied fields E_a spanning three decades from 0 to 3000 V cm^{-1}. The range of applied field, imaging frame rate, image size, and number of images recorded in each experiment, varied depending on the purpose of the data. For the experiments used to determine the critical electric fields, we slowly varied the applied field E_a (defined in equation (3.26)) from an initial low field, corresponding to a stable base state, to a field 333 V cm^{-1} greater than the initial field in 100 increments spaced by

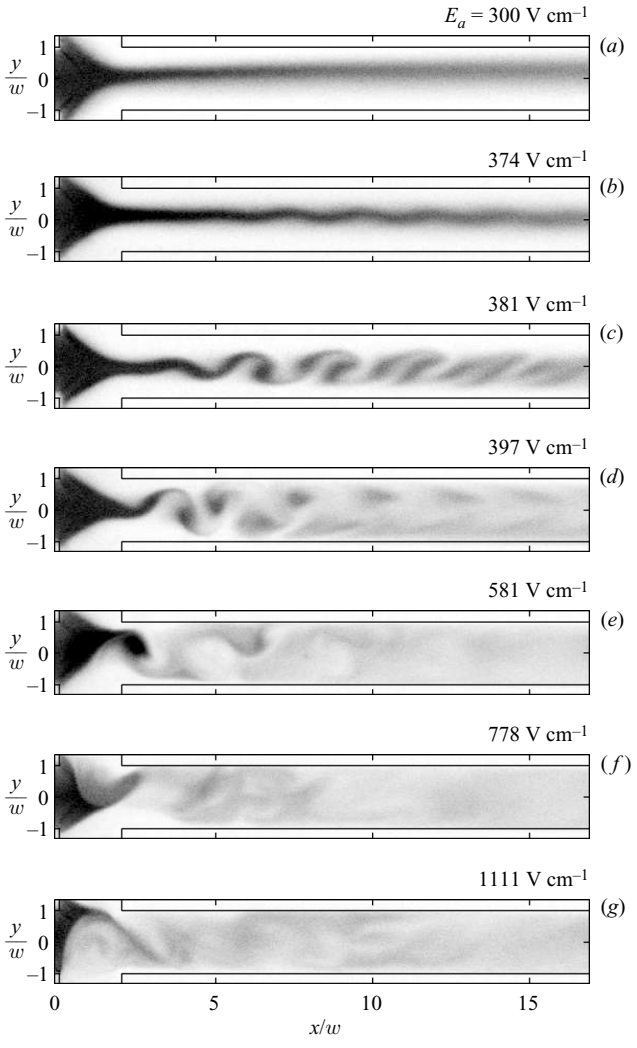

FIGURE 4. Representative instantaneous scalar concentration field, $C_j(x, y)$, images of unstable electrokinetic flow in 50 μm cross-shaped microchannel for centre-to-sheath conductivity ratios $\gamma > 1$ (high conductivity in centre stream). Images correspond to centre-to-sheath conductivity ratio of $\gamma = 100$, applied field ratio of $\beta = 1.13$, and nominal fields E_a noted above each image. The dyed centre stream flows from the west (left) channel and background electrolyte sheath streams flow from the north (top) and south (bottom) channels forming two conductivity interfaces and pinched 'throat' at the intersection. The north and south channels define the intersection that starts at $x/w = 0$ and ends at $x/w = 2$. For stable flow regimes (*a*), the nominal width of the dyed centre stream downstream of the triangle-shaped 'head' is a function of β and γ as well as electrolyte chemistry. (*b*) For applied electric fields above a critical value, a sinuous pattern in the dye develops and grows as it advects downstream. (*c*) At $E_a = 381\ \mathrm{V\,cm^{-1}}$, disturbances grow rapidly as they convect downstream and roll up into alternating flow structures. At still higher electric fields (*d*, *e*, *f* and *g*), the source of the disturbances moves upstream and approaches the origin of the conductivity interface at $x/w = 0$. At high fields, the upstream head structure of the injection stream oscillates in the spanwise direction and modulates the downstream flow. The qualitative nature of the instability does not vary with γ, but the applied field required to reach each flow regime depends on this value and the applied field ratio β.

Exp.	γ	β	E_a (V cm^{-1})	ΔE_a (V cm^{-1})
1†	0.01	0.90	0–3000	56
2†	0.02	0.90	300–3000	56
3†	0.05	0.90	300–3000	56
4†	0.10	0.90	300–3000	56
5†	0.15	0.90	300–3000	56
6†	0.20	0.90	300–3000	56
7†	0.33	0.90	300–3000	56
8†	1.0	1.26	300–3000	56
9†	3.0	1.26	300–3000	56
10	5.0	1.26	444–777	3.33
11	6.0	1.26	444–777	3.33
12	8.0	0.84	333–666	3.33
13	8.0	0.90	333–666	3.33
14	8.0	0.99	333–666	3.33
15	8.0	1.01	333–666	3.33
16	8.0	1.08	333–666	3.33
17	8.0	1.13	333–666	3.33
18	8.0	1.20	333–666	3.33
19	8.0	1.26	333–666	3.33
20	8.0	1.33	333–666	3.33
21	8.0	1.40	333–666	3.33
22	8.0	1.58	333–666	3.33
23	10	1.25	278–611	3.33
24	20	1.25	278–611	3.33
25	50	0.90	278–611	3.33
26	50	1.13	278–611	3.33
27	50	1.35	278–611	3.33
28	50	1.58	278–611	3.33
29	100	0.84	278–611	3.33
30	100	0.90	278–611	3.33
31	100	0.96	278–611	3.33
32	100	1.01	278–611	3.33
33	100	1.08	278–611	3.33
34	100	1.14	278–611	3.33
35	100	1.20	278–611	3.33
36	100	1.26	278–611	3.33
37	100	1.33	278–611	3.33
38	100	1.40	278–611	3.33
39	100	1.58	278–611	3.33
40	100	1.26	333–1122	11.11
41‡	100	1.26	333–1122	11.11

† Manual HVS. Not all fields tested in range.
‡ Image size: 3 × 512, 2000 images recorded at 390 frames per second. Recorded four data sets at this condition.

TABLE 3. Experiments performed. All experiments were conducted with an automated high-voltage sequencer (LabSmith, Livermore, CA, USA) unless otherwise noted. For each case, 200 images were recorded with 100×500 pixel resolution at 115 frames per second, unless otherwise noted. Seven of these experiments were repeated four or more times to ensure reproducibility.

3.33 V cm^{-1}. The initial field for each experiment varied because the critical applied field for instability depends strongly on γ and β. In experiments used to determine critical applied electric field, we recorded 200 images (100 × 512 pixels) at each applied field at a rate of 115 frames per second. All images were recorded with a

Variable	Range
$\gamma = \sigma_W/\sigma_S$	0.01–100
β	0.7–1.5
E_a	0–3000 V cm^{-1}

TABLE 4. Range of independent experimental parameters.

1 ms exposure time. In other experiments, smaller regions of interest are used and images are recorded at higher frame rates. A comprehensive list of the experiments and conditions is show in table 3 and summarized in table 4. In addition to this systematic variation, approximately seven of the experiments were realized four or five times to ensure repeatability across realizations and chip systems.

Before each experiment, the chip microchannels were flushed with a 10 mM solution of sodium hydroxide (NaOH) for 30 min, then deionized water for 10 min, and then background electrolyte for an additional 10 min. The buffer was then allowed to sit in the channel for at least 30 min before each experiment. In this paper, we present data from experiments performed on a single glass chip over the course of twenty weeks. In all cases, the flow required a fraction of a second to become statistically stationary after a change in applied voltage. Image acquisitions began 1 s after a change in applied voltage. The elapsed time for each experiment was approximately 4.5 min. The electrical potential applied at each of the four wells was recorded for all experiments. We filled each reservoir with an equal volume of solution in an effort to initiate each experiment with negligible pressure gradient. As a check, before each experiment, we electrokinetically injected a plug of dye into the east channel, grounded all channel reservoirs, and observed its development for 15 s (a nearly stationary peak indicating negligible pressure gradient). We adjusted the liquid levels of the reservoirs until the plug exhibited no bulk motion.

As discussed in § 5.8, the critical applied electric fields for $\gamma < 1$ (lower conductivity in the centre stream) are much larger than those for $\gamma > 1$. These experiments require larger applied potentials and are conducted with a manual power supply (as denoted in table 3). For these experiments, increments in the applied field were spaced by 56 V cm^{-1}. The larger electrical potentials result in larger flow rates and increased current density. These higher flow rates therefore limited experimental run time owing to fouling of the channel intersection, entrainment of electrolysis bubbles, and unbalancing of channel well heights. Increased current density also led to electrochemical bleaching of the rhodamine B dye (see Jain, Sharma & Bhargava 2003). These effects make experiments time-consuming and expensive, and so we will present only limited data for the $\gamma < 1$ case.

5. Results and discussion

In this section we describe the base state and the qualitative features of the unstable flow fields. We present quantitative results reduced from the scalar images and show how the critical applied field required for unstable flow depends on the conductivity ratio, γ and the applied field ratio controlling centre stream width, β. We end the section with a comparison of local electric Rayleigh number and experimental data and a scalar spectral analysis.

5.1. *Base state flow and centre stream width*

We first present a characterization of the base state flow. Figure 4(*a*) shows the stable flow scalar field for $\gamma = 100$, $\beta = 1.13$ and $E_a = 300$ V cm^{-1}. The dyed centre stream

flows from the west channel and sheath streams flow from the north and south channels forming a pinched throat within the channel intersection. The north and south channels define the intersection that starts at $x/w = 0$ and ends at $x/w = 2$ (see figure 1*b*). For stable flow regimes, the nominal width of the dyed centre stream in the east channel is a function of β and γ as well as electrolyte chemistry. The electrolyte chemistry influences the stream width through the electro-osmotic mobilities of the channels, as described by equation (3.25). We define the measured spanwise (y-direction) half-width of the focused sample stream as the half-width at half-maximum intensity at a downstream location of $x/w \approx 1.5$. This definition of h is consistent with the one-dimensional Green's function solution model presented in § 3.2 where the centre stream and sheath widths are larger than the diffusion thickness δ. Using eleven values of β (experiments 29–39 in table 3) at $\gamma = 100$ and $E_a = 278\,\mathrm{V\,cm^{-1}}$, we determined a least-squares linear fit of the centre stream width normalized by the channel half-height as a function of the field ratio:

$$\frac{h}{w} = 0.97\beta - 0.67, \tag{5.1}$$

where w is the channel half-height. The linear fit results in a linear regression coefficient of $R^2 = 0.94$. For $\gamma = 8$ and $E_a = 333\,\mathrm{V\,cm^{-1}}$ (experiments 12–22), the fit of the centre stream width is

$$\frac{h}{w} = 0.85\beta - 0.57, \tag{5.2}$$

This linear fit results in $R^2 = 0.93$. In § 5.8, we will use these expressions relating field ratio β to constriction of the centre stream in order to scale charge density as a function of the local maximum conductivity gradients. For a given value of the field ratio β, the centre stream will be wider for $\gamma < 1$ than for $\gamma > 1$, as shown in figure 5(*a*). This is due to the dependence of the electro-osmotic mobility on concentration of ions in solution.

5.2. *Unstable flow field*

Next, we describe qualitative features of the onset of the instability. Images of corrected scalar concentration for $\gamma = 100$ and $\beta = 1.13$ recorded at seven applied fields are shown in figure 4. When the applied electric field E_a exceeds a critical value, a sinuous pattern in the dye develops and grows as it advects downstream, as shown in figure 4(*c*) for $E_a = 381\,\mathrm{V\,cm^{-1}}$. For electrical fields corresponding to marginally unstable flow, $E_a = 374\,\mathrm{V\,cm^{-1}}$, small disturbances are detected, but the disturbance amplitude diminishes in size and strength as they convect downstream. With an increase of less than 2% of the applied field, $E_a = 381\,\mathrm{V\,cm^{-1}}$, the disturbances grow exponentially as they convect downstream. Further downstream, the disturbances roll up in alternating sequences, qualitatively similar in appearance to the well-known Bénard–von Kármán vortex street (see Bénard 1908; von Kármán 1912), although in our experiments the nonlinear flow dynamics and formation of coherent structures is driven by electrical body forces and not inertia.

At fields in excess of the critical applied field, $E_a = 397\,\mathrm{V\,cm^{-1}}$, the disturbances grow rapidly, forming coherent structures that originate from near the pinched throat at $x/w \approx 1.5$, as shown in figure 4(*d*). The position of the thin centre stream 'tail', downstream of the throat, periodically fluctuates along the vertical (spanwise) direction and is shown above the x-axis of the channel in this instantaneous image. The source of disturbances moves upstream of the throat to the triangular

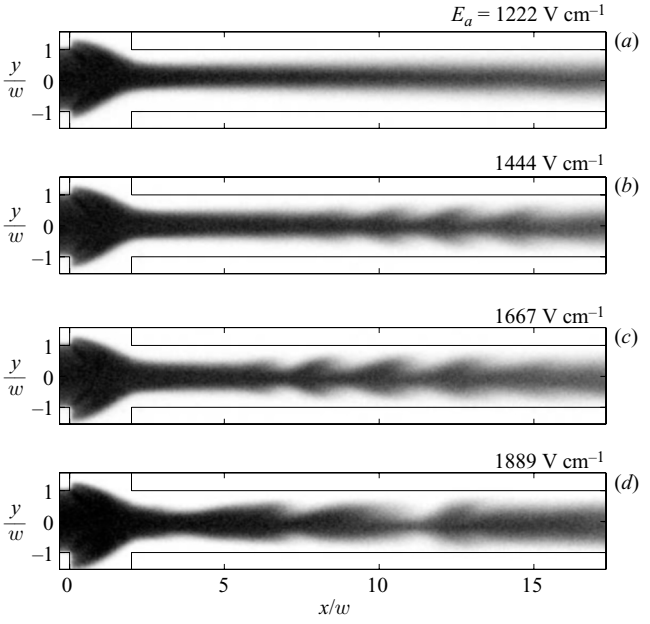

FIGURE 5. Representative instantaneous scalar concentration field, $C_j(x, y)$, images of unstable electrokinetic flow for $\gamma < 1$ (lower conductivity in centre stream). Images correspond to centre-to-sheath conductivity ratio of $\gamma = 0.2$, an applied field ratio of $\beta = 0.9$, and the applied fields, E_a, noted above each image. Although the value of β is smaller for this experiment then for those shown for $\gamma > 1$ (figure 4), the nominal spanwise centre stream width is larger owing to the relatively higher electro-osmotic mobility of the west channel solution. (*b*) For $\gamma < 1$, dilational disturbances grow and convect downstream above a critical value of the electric field. (*c*) The origin of the disturbances moves upstream to $x/w = 6$ as we increase the applied field. (*d*) With a further increase in the applied field, disturbances are readily apparent at $x/w = 3$, are irregularly spaced, and appear to contain multiple wavenumbers.

shaped head at $E_a = 581\,\mathrm{V\,cm^{-1}}$. At this field, the head oscillates in the spanwise direction modulating the downstream flow. At higher fields, $E_a = 778\,\mathrm{V\,cm^{-1}}$, the location of strong disturbances moves further upstream and we observe aperiodic scalar structures and rapid dispersion in the channel. With further increase in the field, $E_a = 1111\,\mathrm{V\,cm^{-1}}$, the source of disturbances moves back to the origin of the conductivity interface at $x/w = 0$. At these applied fields, the throat is a thin filament that rapidly and aperiodically oscillates along the spanwise direction. The dye appears well mixed just downstream of the intersection, at this field. The images shown in figure 4 are a representative sample of the flow patterns that develop for values of $\gamma > 1$. The qualitative nature of the instability does not vary with γ, but the applied field required to reach each flow regime depends on the conductivity ratio and applied field ratio β, as will be discussed in § 5.8. The scalar structures and periodic shedding events visualized in figure 4 show that this flow has a rich spectral signature. Both the spatial and temporal spectral content of scalar fluctuations is discussed in § 5.9.

In the $\gamma < 1$ case (a centre sample stream with a lower conductivity than the sheath streams), we observe spatially periodic dilational flow structures in the unstable flow region, as shown in figure 5. Figure 5 shows representative instantaneous scalar images for $\gamma = 0.2$, $\beta = 0.9$, and four applied fields denoted in the figure. Figure 5(*a*) is the stable base state with an applied field of $E_a = 1222\,\mathrm{V\,cm^{-1}}$. Although the value of

γ is smaller for this experiment than for those in figure 4, the nominal spanwise centre stream width is larger. The larger centre stream width is due to the relatively higher electro-osmotic mobility of the west channel (with respect to the north and south channels), which is in contact with the low ion concentration sample stream solution. For $\gamma < 1$, dilational disturbances grow and convect downstream when the critical electric field is exceeded, $E_a = 1444\,\mathrm{V\,cm^{-1}}$, as shown in figure 5(*b*). As we increase the applied field to $E_a = 1667\,\mathrm{V\,cm^{-1}}$, the source of disturbances moves upstream to $x/w = 6$ as shown in figure 5(*c*). With a further increase in the applied field to $E_a = 1889\,\mathrm{V\,cm^{-1}}$, disturbances are readily apparent at $x/w = 3$, as shown in figure 5(*d*). At this field, the disturbances are irregularly spaced and appear to contain multiple wavenumbers. Note that, in figures 5(*c*) and 5(*d*), the head is slightly asymmetric about the x-axis (bottom side larger than the top side) as the potential to the south well was limited by the 6000 V maximum of our high-voltage power supply.

5.3. *Statistical moments of scalar images*

Next, we present average and perturbation dye concentration fields for $\gamma > 1$. The first moment (mean concentration field) is calculated as,

$$\overline{C(x, y)} = \frac{\sum_{j=1}^{n} C_j(x, y)}{(n-1)}, \tag{5.3}$$

where n is the number of images. The averages are calculated over $n = 200$ images and shown in figure 6. For the experimental conditions used in this paper, the speed at which the disturbances convect downstream is too fast for the human eye to resolve the flow structures. For this reason, the average scalar fields are comparable to what we see through the microscope binoculars when running the experiments. The mean field images shown in figure 6 correspond to the same conditions as for those shown in figure 4. Below the critical applied field, $E_a = 300\,\mathrm{V\,cm^{-1}}$, the centre stream remains in a thin filament and diffuses slowly in the spanwise direction. Above the critical applied field, $E_a = 381\,\mathrm{V\,cm^{-1}}$, the centre stream is dispersed by low-amplitude disturbances and appears to be slightly widened in this average concentration image, as shown in figure 6(*c*). At $E_a = 397\,\mathrm{V\,cm^{-1}}$, disturbances grow in amplitude, and their point of origin moves to the throat at $x/w \approx 1.5$. At this field, the envelope of high-intensity concentration widens quickly and the centreline scalar value decreases exponentially along the streamwise direction. At higher fields, the source of disturbances moves further upstream and results in a highly dispersed scalar field, as shown in figure 6(*e–g*).

Figure 7 shows mean square scalar perturbation fields for the $\gamma = 100$, $\beta = 1.13$ and the fields shown in figure 4. At each condition, the mean square perturbation is defined as,

$$\overline{C'(x, y)^2} = \frac{\sum_{j=1}^{n} C'_j(x, y)^2}{(n-1)}, \tag{5.4}$$

where the scalar perturbation is $C'_j = C_j(x, y) - \overline{C(x, y)}$. Figure 7(*a*) shows the stable base state perturbation field recorded at $E_a = 300\,\mathrm{V\,cm^{-1}}$. Figure 7(*b*) shows the marginally unstable flow in which two thin streamwise-oriented regions of disturbance

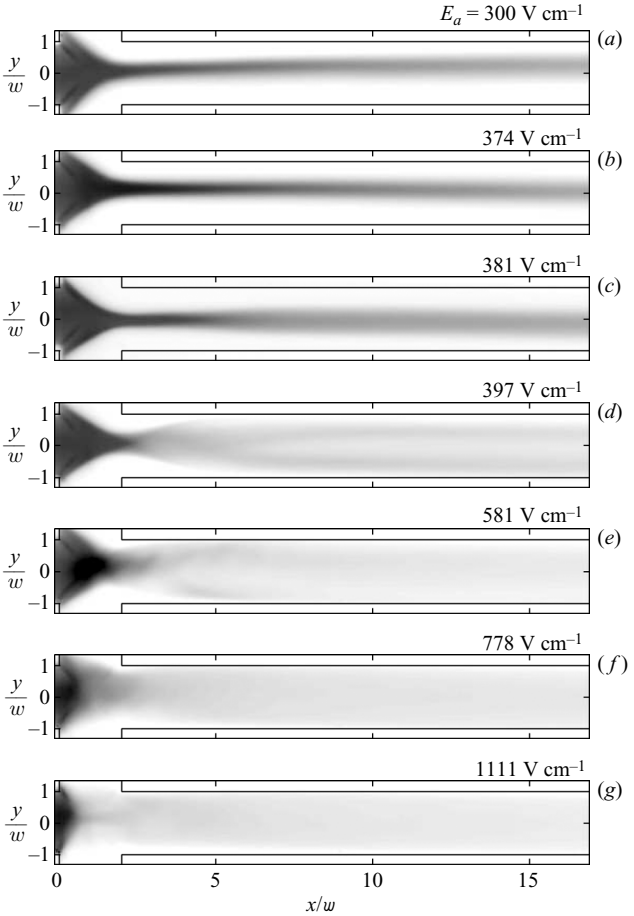

FIGURE 6. Average scalar fields, $\overline{C(x, y)}$, for $\gamma = 100$, $\beta = 1.13$, and the applied fields noted above each image (same conditions as the experiments of figure 4). For the experimental conditions used in this paper, the speed at which imaged disturbances convect downstream is too fast for the human eye to resolve flow structures (even with lower magnification optics). For this reason, these average scalar fields are comparable to what we see through our microscope binoculars when running experiments. (*a*) Below the critical applied field, the centre stream remains in a thin filament and diffuses slowly in the spanwise direction. (*c*) Above the critical applied field, the centre stream is dispersed by low-amplitude disturbances and appears slightly widened in this average concentration image. (*d–g*) At higher fields, the origin of the disturbances moves further upstream and strong fluctuations result in highly dispersed scalar fields.

originate at the downstream position of $x/w = 5$ and die out near $x/w = 10$. The perturbations grow in strength and the location of strong perturbations moves upstream, as the field increases (figure 7*c–g*). At $E_a = 397\,\mathrm{V\,cm^{-1}}$ (figure 7*d*), the point of origin of the perturbations has moved back to the throat at $x/w \approx 1.5$. The spanwise growth of the perturbation envelope is approximately exponential until this width is bounded by the channel walls as shown in figure 7(*d*). The spatial growth rates of the perturbation fields will be discussed in § 5.6. For now, we will note that perturbations are observed to be convective in nature and grow in space as $\hat{C}\mathrm{e}^{-K(x/w)}$, where the non-dimensional (channel half-height) growth rate is $-K$. As the applied

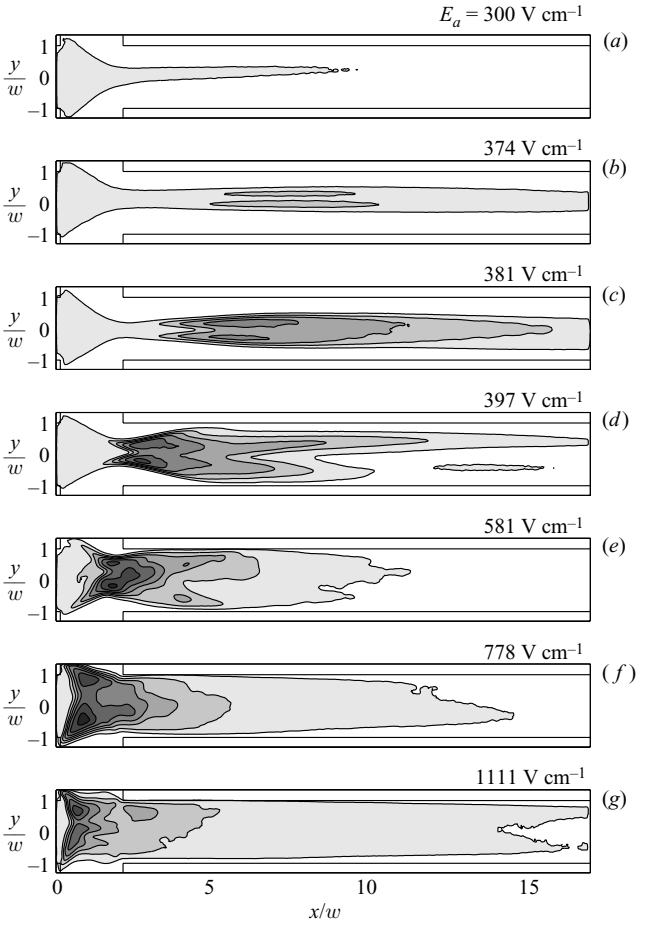

FIGURE 7. Mean scalar perturbation fields $\overline{C'(x,y)^2}$ for $\gamma = 100$, $\beta = 1.13$, and the applied fields given above each image (the conditions of the experiments are as in figure 4). The contours are spaced by an interval $\Delta\overline{C'(x,y)^2} = 0.05$ and the white regions have a value of zero. (*a*) The stable base state has minimal perturbation values throughout the flow field. (*b*) For a marginally unstable flow, two thin streamwise-oriented regions of disturbance originate at the downstream position of $x/w = 5$ and these die out near $x/w = 10$. (*c*, *d*) As the field increases, perturbations grow in strength and their point of origin moves upstream. (*f*) At $E_a = 778\,\mathrm{V\,cm^{-1}}$, the triangular-shaped head begins to oscillate strongly along the vertical direction and the source of disturbances moves back towards the origin of the conductivity gradient at $x/w \approx 0$. (*g*) At $E_a = 1111\,\mathrm{V\,cm^{-1}}$, the region of strongly perturbed flow shortens and the pertubation field is characterized by very strong fluctuations near the point $x/w \approx 0$. (*e–g*) At fields above $581\,\mathrm{V\,cm^{-1}}$, the flow is strongly unstable and well mixed downstream of $x/w \approx 5$.

field increases further, the source of the perturbations moves upstream of the throat, $x/w < 1.5$, to the region originally occupied by the triangle-shaped injection head, as shown in figure 7(*e–g*). At $E_a = 778\,\mathrm{V\,cm^{-1}}$ (figure 7*f*), the injection head moves periodically in the vertical direction and the location of strong perturbations moves back towards the origin of the conductivity gradient at $x/w \approx 0$. At $E_a = 1111\,\mathrm{V\,cm^{-1}}$ (figure 7*g*), the region of strongly disturbed flow shortens and the scalar structure is characterized by very strong fluctuations near the point $x/w \approx 0$. At fields above

$E_a = 581\ \mathrm{V\,cm^{-1}}$ (figure 7*e–g*), the flow is highly unstable, and downstream of $x/w = 5$, the flow is well mixed.

5.4. *Velocity fields*

In this section, we present estimates of the convective velocity of structures in the unstable flow regime of the flow. We infer the streamwise ensemble-average velocity of the flow in the east channel by tracking the displacement of scalars. Note that the bulk flow velocity in the east channel is difficult to quantify using bulk measurement methods such as current monitoring (see Huang, Gordon & Zare 1988; Ren, Escobedo & Li 2001; Devasenathipathy & Santiago 2005) as the flow has highly non-uniform conductivity and electric fields, resulting in non-uniform unsteady electro-osmotic velocities near the walls. Only optical flow structure (or seed particle) tracking methods are possible. Velocity in microchannels has been measured using micron resolution particle image velocimetry (μPIV) in pressure-driven flows (see Santiago *et al.* 1998; Meinhart, Wereley & Santiago 1999; Cummings 2000) and electrokinetic flows (see Devasenathipathy, Santiago & Takehara 2002). Velocity fields of electrokinetic flows in microchannels have also been inferred from tracking the displacement of lines of maximum concentration of photo-activated caged dyes (see Sinton & Li 2003). Note that the tracking of charged species (as in the case of particles typically used in PIV) is greatly complicated because such seeded species experience wildly fluctuating non-uniform electrolyte chemistries as they move through the EKI flow field.

In this study, we use cross-covariance from two successive images, recorded 8.7 ms apart, to determine the displacement of passive scalar patterns. Measuring velocity using correlations of successive scalar images has been investigated in more standard fluid flows (see Tokumaru & Dimotakis 1995; Koochesfahani, Cohn & McKinnon 2000). Our algorithm discretizes the image pairs into regularly spaced interrogation regions similar to PIV algorithms (see Adrian 1991). The displacement in each interrogation region is calculated from the ensemble average of cross-covariances. We ensemble averaged the correlations of 50 image pairs to improve the signal-to-noise ratio in determining the displacement peak (see Santiago *et al.* (1998) for a discussion of ensemble averaging of cross-covariances). The displacement is determined with sub-pixel displacement resolution by fitting a five-point Gaussian curve to the ensemble-averaged correlation function. As this technique requires streamwise gradients in scalar concentration, we are restricted to the quantification of velocities in unstable flow conditions.

Figure 8 shows spanwise velocity profiles for $\gamma = 100$, $\beta = 1.13$ and $E_a = 425\ \mathrm{V\,cm^{-1}}$ for four streamwise locations. The interrogation windows are 100 pixels wide and 6 pixels in height with a 50% window overlap. Several flow features are revealed by the analysis. The velocity at the wall is non-zero owing to the electro-osmotic slip velocity. At $x/w = 2.5$, the velocity profile is broad with a small inflection at the spanwise midline, $y/w = 0$. The local minimum at the centre of the profile is caused by the lower velocity of the high-conductivity centre solution. Recall that electro-osmotic mobility decreases with increasing ion density. Further downstream, the velocity profile is less 'plug like' and develops a peak near the centre half of the channel. Although our control volume analysis predicts favourable pressure gradients in the east channel, this simple analysis does not account for a strongly pronounced peak in the velocity profile. This profile shape is most probably due to the effects of counter-rotating flow structures observed in this strongly unstable flow field. See for example, at $E_a = 397\ \mathrm{V\,cm^{-1}}$ in figure 4(*d*), where strong coherent flow structures are alternately shed in a periodic deterministic fashion.

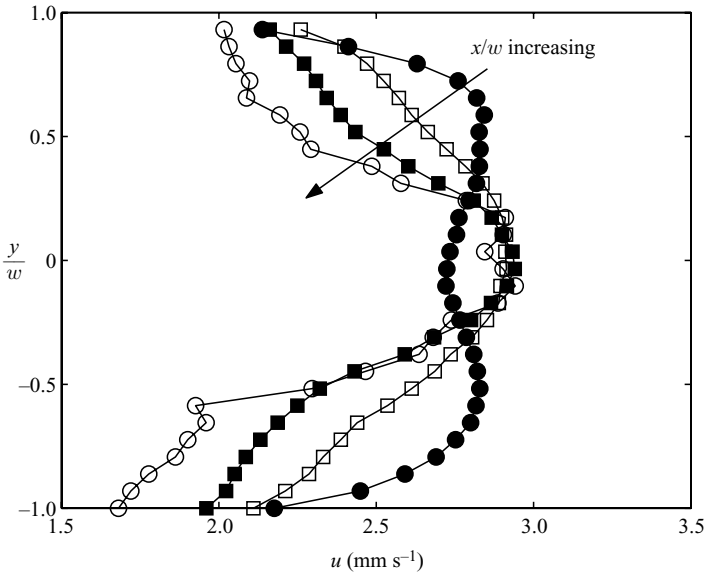

FIGURE 8. Spanwise velocity profiles for $\gamma = 100$, $\beta = 1.13$, $E_a = 425\,\mathrm{V\,cm^{-1}}$, and four downstream locations ●, $x/w = 2.5$; □, 3; ■, 3.5; ○, 4. The streamwise ensemble average velocity of the flow in the east channel is estimated by tracking the displacement of scalars using cross-covariances of successive image pairs. The velocity at the wall is non-zero owing to the electro-osmotic slip velocity. At $x/w = 2.5$, the velocity profile is broad with a small inflection at the spanwise midline $y/w = 0$. The inflection is probably due to the reduced electro-osmotic mobility associated with the high-conductivity centre stream which contacts the top and bottom surfaces of the microchannel (at $z/d = 0$ and 1). Further downstream, the velocity profile is less 'plug like' and develops a peak near the centre half of the channel. Spanwise integration of velocity profiles provides a measure of the volume flux through the microchannel. The volume flux calculated from each velocity profile is within 8% of the mean value of all profiles.

Spanwise integration of velocity profiles provides a measure of the volume flux through the microchannel. The estimated volume flux is uniform along the streamwise direction as expected. The volume flux calculated from each velocity profile is within 8% of the mean value of all profiles. From these fluxes, we can determine the area averaged velocity as a function of the applied field. For $\gamma = 100$, $\beta = 1.13$, and using velocity profiles at $x/w = 2.5$, the area average velocity varies as $U = 4 \times 10^{-6} \times E_a\,\mathrm{m\,s^{-1}}$ (E_a in units of $\mathrm{V\,cm^{-1}}$) (with an R^2 value of 0.95).

5.5. *Perturbation energy measurements*

The origin, spatial distribution and amplitude of scalar perturbations depend on the applied field and the conductivity ratio. Figure 9 shows maps of scalar perturbation versus applied field and downstream location for four values of $\gamma = 6, 8, 50, 100$ and $\beta = 1.13$. We construct these plots from spanwise averages (from $y/w = -1$ to 1) of scalar perturbation fields as measured from 200 instantaneous images and at each of 100 applied electric fields. For each value of γ there is a critical applied field 'rise' at which the perturbation energy increases rapidly downstream of the throat at $x/w > 1.5$. For example, at $\gamma = 6$ in figure 9(*a*), the perturbation energy grows sharply at $E_c \approx 525\,\mathrm{V\,cm^{-1}}$ and plateaus to a 'shelf' with increasing applied field and downstream location. For a small increase in the conductivity ratio to $\gamma = 8$, the sharp increase in critical applied field moves down to $E_c \approx 425\,\mathrm{V\,cm^{-1}}$. At this

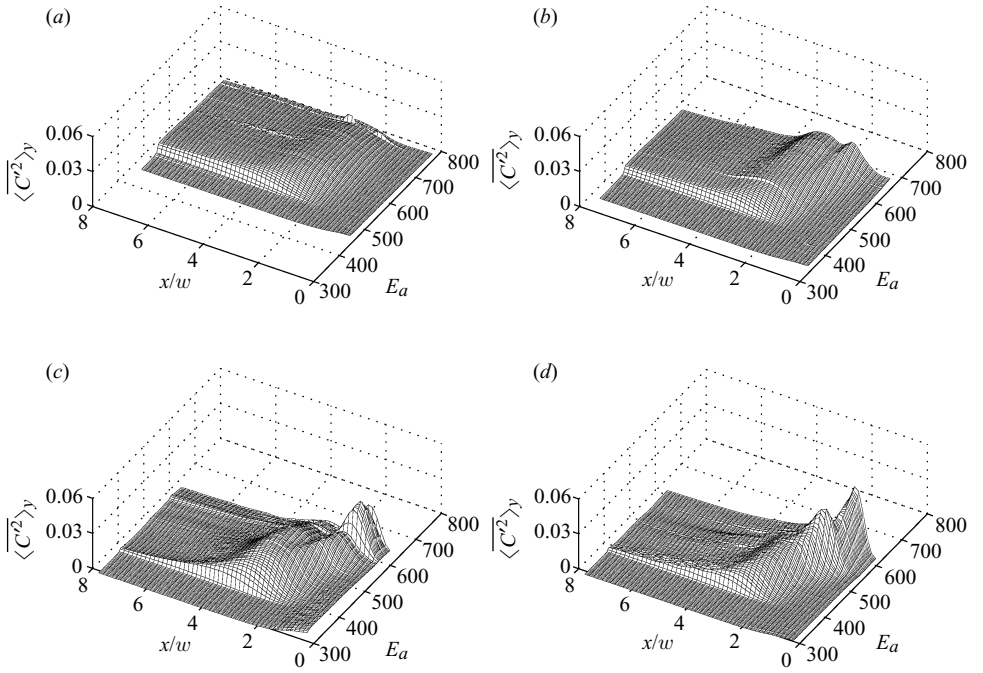

FIGURE 9. Space-field maps of scalar perturbation energy $\langle\overline{C'^2}\rangle_y$ as a function of nominally applied field, E_a, and streamwise location, x/w. Measurements are shown for $\beta = 1.13$ and conductivity ratios of $\gamma = 6$, 8, 50 and 100. For each γ value, there is a sharp increase in perturbation energy versus electric field profiles for regions downstream of the throat ($x/w \approx 1.5$). This sharp increase marks the critical electric field for the onset of the instability. For relatively low γ (a, $\gamma = 6$; b, $\gamma = 8$), the perturbation energy plateaus to a shelf for regions above the critical applied field and downstream of $x/w \approx 1.5$. For higher γ (c, $\gamma = 50$; d, $\gamma = 100$), a wide ridge of large perturbation energy develops at $x/w \approx 3$ and a narrower ridge develops at $x/w \approx 0.9$. These two ridges are associated with the vertical oscillatory motion of the centre stream throat and head structures, respectively (see figures 4d and 4e). At $\gamma = 50$ and 100, the perturbation energy shelf in the supercritical-field regime decays downstream indicating that the rapid upstream fluctuations of the flow have quickly dispersed the dye into a well-mixed state.

conductivity ratio, we begin also to clearly discern regions of increased energy for supercritical applied fields. These regions appear as a wide ridge centred at $x/w \approx 3$ and a thinner ridge at $x/w \approx 0.9$. These broad and sharp ridges are associated with the strong vertical oscillatory motion of the centre stream throat and head structures, respectively (see figure 4e). The perturbations are especially strong at these upstream locations owing to the existence of sharp gradients in dye tracer not yet dispersed by molecular diffusion and electroviscous stirring. At $\gamma = 50$, the perturbation energy shelf in the supercritical applied field region decays rapidly downstream of about $x/w = 4$, indicating that the rapid fluctuations of the upstream perturbation ridges have dispersed the dye into a well-mixed state. At this value, the broad ridge is substantially reduced in intensity compared to the sharp upstream ridge which has grown in intensity. At the highest conductivity ratio that we tested, $\gamma = 100$, the broad downstream ridge disappears and only the sharp, upstream ridge remains. At this highest value, the energy rapidly decays downstream of the throat for fields above the critical value $E_c \approx 380\,\mathrm{V\,cm^{-1}}$. The latter behaviour of the perturbation energy map at high γ and E_a is associated with rapid mixing within the intersection and a well-mixed state just downstream of the intersection.

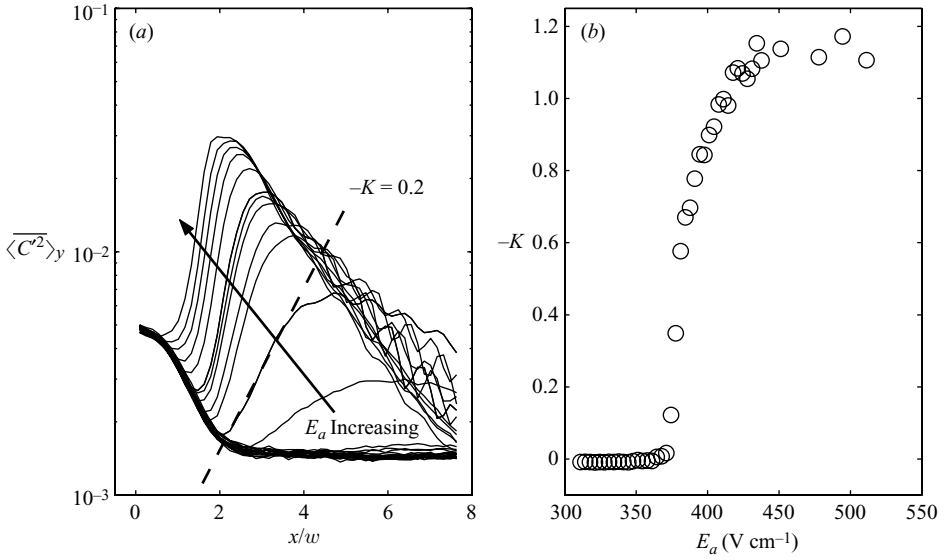

FIGURE 10. (*a*) Spanwise-averaged scalar perturbation energy, $\langle\overline{C'^2}\rangle_y$, as a function of the streamwise location for $\gamma = 100$ and $\beta = 1.13$. The baseline of the perturbation energy decreases from $x/w = 0$ to 2. This region directly maps to the flow region occupied by the triangular-shaped injection head at stable conditions. For stable flows, the perturbation energy remains at a constant value of 1.5×10^{-3} for x/w values larger than 2. The perturbation energy grows exponentially in space for unstable flow. The straight portion of these log–linear curves indicates an exponential growth in space. The slopes of the perturbation energy profiles are the exponential growth rates $-K$ for each field, and these are shown in (*b*). The growth rate is near zero for subcritical electric fields. At a critical electric field of $E_c \approx 365\,\mathrm{V\,cm^{-1}}$, the growth rate exhibits a sharp increase and then saturates to a value of $-K = 1.2$.

Together, the perturbation surface plots of figure 9 capture the salient qualitative features of the flow, including the existence of a strong critical applied field for each γ; the mixing effect of strong upstream perturbations at large electric field and γ; and the movement of the source of perturbations upstream for increasing field. In the next sections, we will explore each of these effects more closely and compare these experimental trends to the predictions of our simple scaling models.

5.6. *Spatial growth rates*

Linear perturbation theory predicts exponential growth of perturbations of the form $\hat{C}e^{-K(x/w)}$ for convective electrokinetic instabilities (see Chen *et al.* 2005). Chen *et al.* (2005) measured regions of exponential spatial growth for convective instability in a high-aspect-ratio T-shaped microchannel. They analysed the distribution of spanwise-averaged perturbation amplitude (scalar perturbation energy) with increasing streamwise coordinate of their flow. We shall take a similar approach here. This definition is consistent with the $\mathrm{d}/\mathrm{d}(x/w)$ slope of the perturbation energy surfaces shown in figure 9. Figure 10(*a*) shows curves of spanwise-averaged scalar perturbation energies $\langle\overline{C'^2}\rangle_y$ as a function the streamwise location x/w for applied fields between 278 and 500 $\mathrm{V\,cm^{-1}}$. The baseline of the perturbation energy decreases from $x/w = 0$ to 2 for fields below $E_a = 350\,\mathrm{V\,cm^{-1}}$. This decay for low fields directly maps to the stable flow in the region occupied by the triangular-shaped injection head. When the flow is stable, the perturbation energy remains at a constant value of 1.5×10^{-3} for x/w values larger than 2.

The spatial exponential growth of perturbation energy is clearly apparent for electric field values above $365\,\mathrm{V\,cm^{-1}}$. At these higher fields, the perturbation energy initially follows the baseline decay, but then transitions into a rapidly increasing energy associated with the onset of strong instability. The straight portion of the log–linear curves of figure 10(*a*) indicate an exponential growth in space. For an increasing field, the region of rapid exponential growth (and associated departure from the baseline) moves further upstream as the source of disturbances moves upstream. In all cases, the perturbation energy increases to a peak value and then decreases via a single decaying exponential at higher x/w. The location of this peak moves upstream and increases in intensity with increasing field. This peak in energy is indicative of the strength of the disturbances, followed by the subsequent decay in perturbations in the scalar field owing to strong stirring of the flow field. These regions of strong perturbations and well-mixed fluid can be compared to the images shown in figures 4, 7 and 9.

Figure 10(*b*) shows the slope of least-squares linear fits to the perturbation energy growth. The slope of the linear fit is the exponential growth rate $-K$. The growth rate is near zero for subcritical electric fields. At the critical electric field of $E_c \approx 365\,\mathrm{V\,cm^{-1}}$, the growth rate exhibits a sharp exponential increase with the applied field and then saturates to a value of $-K = 1.2$.

The perturbation intensity fields of figure 7 show that the origin of disturbances moves upstream with increasing applied field. At $E_a = 778\,\mathrm{V\,cm^{-1}}$, strong perturbations are observed near the origin of the conductivity interface at $x/w = 0$. This trend is shown more clearly in figures 10(*a*) and 11. Figure 10(*a*) shows spanwise-averaged scalar perturbation energy as a function of the streamwise coordinate. The region of exponential growth of perturbation energy clearly moves upstream with increasing field. The location of maximum perturbation is first evident at $x/w \approx 6$ for electric fields near the critical value and quickly shifts upstream with increasing field. Figure 11 shows the streamwise position x/w of maximum scalar perturbation energy as a function of the applied field E_a for $\gamma = 6$, 8, 50, and 100. The maximum perturbation location is approximately linear with the field at higher fields. For values of $\gamma = 6$ and below, the region of strong perturbations never moves further upstream than $x/w \approx 2.5$. For larger γ values, the source of strong perturbations approaches the origin of conductivity interfaces at $x/w = 0$. From these data, the location of large perturbations appears to be invariant to γ for γ greater than about 50.

The shift of disturbances toward the origin of the conductivity interfaces suggests that the magnitude of the local electroviscous velocity is equal to or larger than the magnitude of the local advective velocity provided by electroosmosis (e.g. resulting in the non-dimensional velocity scale R_v). This observed trend may provide insight to the demarcation between convective and absolute instability in these flows. The concepts of absolute and global instability are commonplace for convective stability models (see for example Huerre & Monkewitz 1990), including convective electrokinetic flows (see Chen *et al.* 2005). The onset of, or transition to, absolute instability is often difficult to detect experimentally (see Huerre & Monkewitz 1990; O'Donnell, Chen & Lin 2001).

5.7. *Dependence on electric field ratio*

In this section, we explore the effect of the centre stream width on the stability of the flow. The width of the centre stream is controlled in the experiments by the applied field ratio β as described in § 4.3. Figure 12 shows contour maps of the area-averaged scalar perturbation energy $\langle \overline{C'^2} \rangle_{xy}$ as a function of the nominally applied field E_a and electric field ratio β for $\gamma = 8$ and 100. Each contour map is rendered from normalized image data at 11 values of β and 100 discrete applied fields E_a. Each of these 1100 experiments provides 200 instantaneous images which are used to calculate

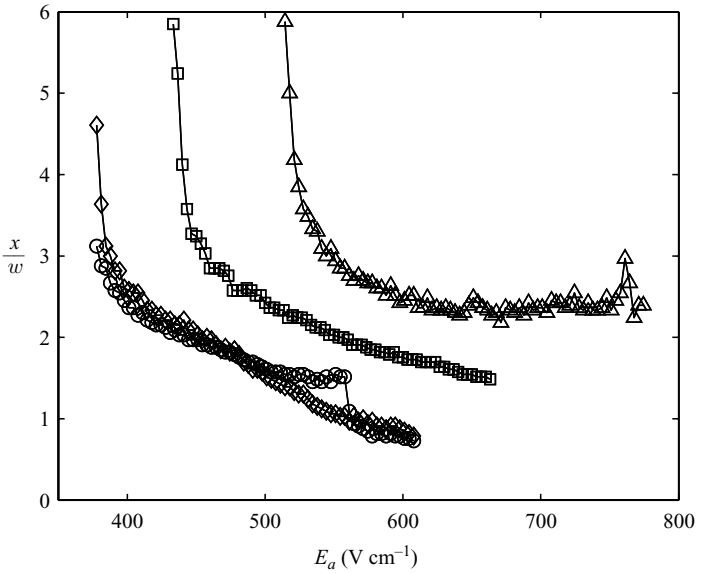

FIGURE 11. Streamwise position of maximum scalar perturbation energy plotted as a function of applied field E_a for △, $\gamma = 6$; □, 8; ○, 50; ◇, 100. The location of maximum perturbation originates at $x/w \approx 6$ for electric fields near the critical value and quickly shifts upstream with increasing field. The maximum perturbation location versus field relation becomes linear at higher fields. For γ values of 6 and below, the location of the region of strong perturbations asymptotes to about $x/w \approx 2.5$. For larger γ, strong perturbations tend towards the origin of conductivity interfaces at $x/w = 0$. In our flow field, the growth of disturbances near the origin of the conductivity interfaces suggests that the local electroviscous velocity produced by electric body forces in the flow exceeds the local magnitude of advective velocity provided by electroosmosis, resulting in absolute instability.

the perturbation fields. Each point in the maps of figure 12, is generated from the area-averaged perturbation over a region of 50×512 pixels circumscribed by $y = -1$ to 1 and $x/w = 0$ to 15.

At each field ratio, the area-averaged scalar perturbation energy increases dramatically at a critical applied field. The perturbations are strongest and the critical applied fields are lowest for β values of about 1.25 for both γ values. We attribute this behaviour to the magnitude of conductivity gradients (and associated electric charge density) as a function of the centre stream width. Note that centre stream width depends solely on β for a given conductivity ratio. At a β of 1.25, the centre stream width is nearly equal to the sheath stream widths (i.e. centre stream takes up approximately one third of the channel) which is apparent from equations (5.1) and (5.2). Larger β values denote wide centre streams with thin sheath flows whose gradients are quickly dispersed by molecular diffusion. Smaller β values are associated with overly narrow centre streams whose conductivity gradients are also quickly dispersed by diffusion. The significance of the conductivity ratio γ and the electric field ratio β on the onset of flow instability are discussed in the next section.

5.8. *Critical conditions for onset of flow instability*

We determined the critical applied field required for instability for each conductivity ratio by slowly ramping the applied field E_a from an initial low value (corresponding to the stable base state) and then analysing fluctuations of scalar intensity as a function of the applied field. In these experiments, we define the critical electric field E_c as the applied field E_a that results in an area-averaged scalar perturbation energy

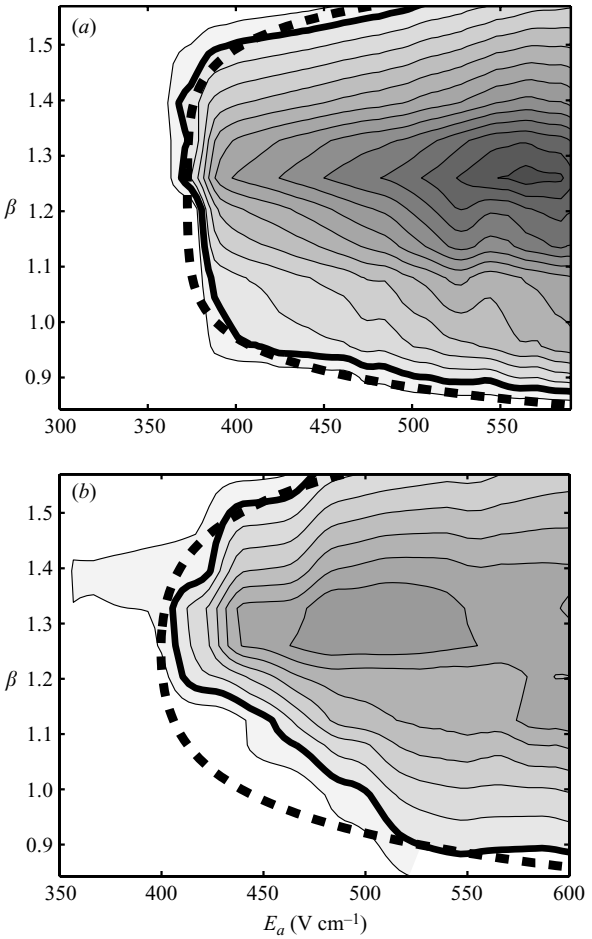

FIGURE 12. Contour maps of $\langle\overline{C'^2}\rangle_{xy}$ plotted as a function of the nominally applied electric field, E_a, and west-to-south applied field ratio, β, for (*a*) $\gamma = 100$ and (*b*) $\gamma = 8$. Each contour map is rendered from normalized image data at 11 values of β and 100 discrete applied fields, E_a. The contours are spaced by an interval of $\Delta\langle\overline{C'^2}\rangle_{xy} = 0.001$ and the white regions have a value of zero. For a given conductivity ratio, β independently controls the width of the centre stream, h. At each field ratio, the area-averaged scalar perturbation energy increases dramatically at a critical applied field. The contour defining the onset of instability ($\langle\overline{C'^2}\rangle_{xy} = 0.002$) is shown as a bold solid line. The critical applied field is lowest for β values of about 1.25 for both γ values. For (*a*) $\gamma = 100$, the critical applied field is nearly constant for β values between about 0.95 and 1.5. We account for the effects of electric body forces, viscous forces and the effects of molecular diffusion using a local electric Rayleigh number scaling. Contours of the critical local electric Rayleigh number (equation (3.19)) $Ra_{e,\ell} = 205$ are plotted as bold dashed lines.

$\langle\overline{C'^2}\rangle_{xy}$ that is twice that of the stable (base) state. Examples of this critical electric field determination are shown in the inset of figure 13. The inset shows a plot of area-averaged scalar perturbation energy as a function of the applied field. For all γ values, the scalar perturbation undergoes a dramatically sharp increase at the critical applied field value. For $\gamma = 100$, the perturbation intensity doubles from the base value of 0.001 to 0.002 at an applied field of $E_a = 365\,\mathrm{V\,cm^{-1}}$. A doubling of the perturbation magnitude occurs within a field increment of just $5.5\,\mathrm{V\,cm^{-1}}$. The critical

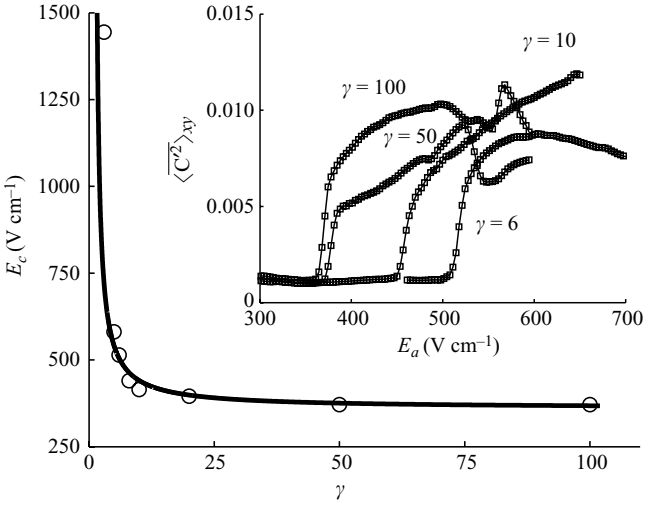

FIGURE 13. Critical applied electric field, E_c, plotted as a function of the centre-to-sheath conductivity ratio for $\gamma > 1$ and $\beta = 1.13$. The inset shows the area-averaged scalar perturbation energy as a function of the applied field for $\gamma = 6$, 10, 50 and 100. The critical applied field is defined as the E_a value at which perturbation energy increases to twice the stable base state value. The main plot shows the critical applied field required for onset of instability as a function of the conductivity ratio. The critical applied field asymptotes to about $E_c = 365\,\mathrm{V\,cm^{-1}}$ at large conductivity ratios and increases rapidly for decreasing γ near $\gamma = 1$. The trend of critical applied field with γ is captured by our scaling analysis of local electric Rayleigh number. The critical applied field required for the onset of instability, equation (5.5), is plotted for $Ra_{e,\ell\,crit} = 205$ as a solid line.

applied field value increases with decreasing conductivity ratio for $\beta = 1.13$. The main plot of figure 13 shows a summary of the critical electric fields as a function of the conductivity ratio. The critical applied field asymptotes to about $E_c = 365\,\mathrm{V\,cm^{-1}}$ at large conductivity ratios, and increases rapidly for decreasing γ near $\gamma = 1$.

The trend of critical applied field with increasing γ is captured by the scaling analysis presented earlier. Our electrokinetic flow field is expected to become unstable at a critical local electric Rayleigh number (see Lin *et al.* 2004; Chen *et al.* 2005). From our relation for a modified local electric Rayleigh number, equation (3.19), we can solve for the critical value of the applied field as a function of a critical Rayleigh number and conductivity ratio γ as follows:

$$E_c = \sqrt{\frac{Ra_{e,\ell\,crit}}{\nabla^*\sigma^*|_{max}} \frac{D\mu}{\epsilon d^2} \frac{\gamma}{\gamma - 1}}. \tag{5.5}$$

Although the centre-stream width varies with γ for a given β, we approximate the value of $\nabla^*\sigma^*|_{max}$ as unity for $\beta = 1.13$ using equations (5.1) and (5.2). This is a reasonable assumption since the value of $\nabla^*\sigma^*|_{max}$ is near unity for a wide range of h values (see the derivation and evaluation of $\nabla^*\sigma^*|_{max}$ in the Appendix). Values of other parameters used in equation (5.5) are given in table 2. This scaling of the critical electric field for $Ra_{e,\ell\,crit} = 205$ is plotted against the experimental data as a solid curve in figure 13. There is good qualitative agreement between the trends predicted by this simple first-order scaling relation and the quantitative experimental data for a modified electric Rayleigh number of 205.

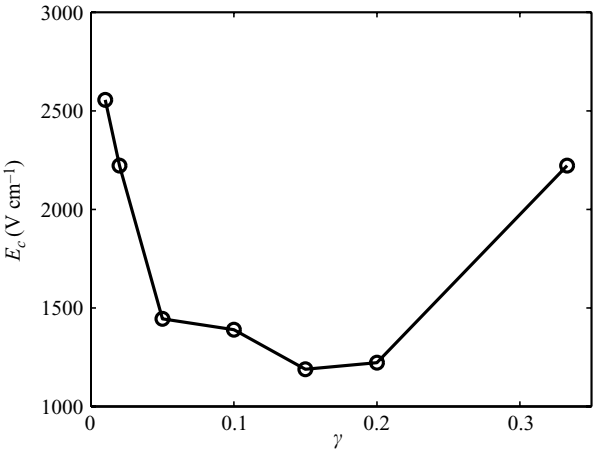

FIGURE 14. Critical applied electric field, E_c, plotted as a function of the centre-to-sheath conductivity ratio for $\gamma < 1$ and $\beta = 0.9$. The critical applied fields are much larger than those for $\gamma > 1$. There is a local minimum for the critical applied field at $\gamma \approx 0.15$. The critical applied field increases rapidly as γ approaches both 0 and 1.0.

Previous EKI studies have also presented scaling analyses and predictions for the critical applied electric field as a function of the conductivity ratio γ. Chen *et al.* (2005) developed scaling for the Rayleigh number as a function of the conductivity gradient, as discussed in § 3.2. This scaling results in a critical applied field dependence of the form $[(\gamma + 1)/(\gamma - 1)]^2$ which also agrees well with our experimental data. The dependence of the critical electric field on the normalized conductivity gradient is different from that predicted by the scaling of Baygents & Baldessari (1998). The latter scaling predicted an inflection point in the field versus gradient curve, with the critical field rising for both the low- and high-conductivity gradient limits.

Using a similar experimental procedure, we have identified the critical electric field for the $\gamma < 1$ experiments (experiments 1 to 7 in table 3). The critical applied fields for $\gamma < 1$ are shown in figure 14. For this range of the conductivity ratio, the critical electric field is much larger in magnitude than the $\gamma > 1$ case. Unexpectedly, we see a local minimum for the critical applied field at $\gamma \approx 0.15$. For this range of γ, there appears to exist two large (perhaps asymptotic) values for the electric field at γ values of 0 and 1.0. Our first-order scaling relations do not account for this variation of the critical applied field in the domain of $\gamma < 1$ and may be the focus of future investigations. One possible cause for this behaviour is the two-dimensional nature of base state electric fields. For the $\gamma < 1$ case (where the centre stream conductivity is low and centre stream electro-osmotic mobility is high), electric fields are expected to emerge from the centre stream and quickly flow into the sheath streams within a few channel widths of $x/w = 0$. This crossing of electric field lines from low to high conductivity regions may have a stabilizing effect on the flow field not present in the $\gamma > 1$ case. Unsteady, three-dimensional simulations of the flow in this region may shed light on the critical applied field versus γ behaviour in these flows.

We again turn back to the more in-depth analysed $\gamma > 1$ case. Figure 15 shows the spatial growth rates for $\gamma = 6$, 8, 20 and 100 where the abscissa is normalized by the critical electric field for each conductivity ratio. The spatial growth rates are shown to collapse when scaled by the critical electric field. This collapse demonstrates that our definition of the critical applied field is equivalent to the field at which the

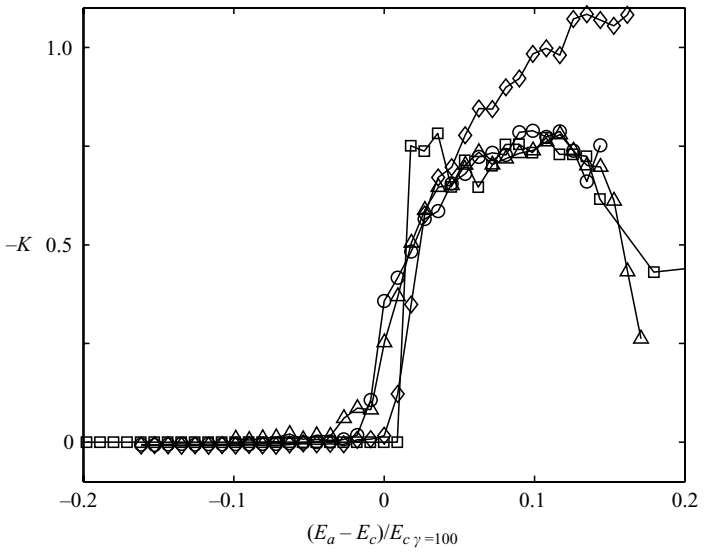

FIGURE 15. Perturbation growth rate slopes $-K$ plotted as a function of the normalized applied field for △, $\gamma = 6$; □, 8; ○, 50; ◇, 100. The growth rates collapse for an applied field normalization of the form $(E_a - E_c)/E_{c,\gamma=100}$. This collapse demonstrates that our definition of the critical applied field is consistent with the field at which the instability exhibits a non-zero growth rate.

instability exhibits a non-zero growth rate. This definition is consistent with the linear convective stability analysis of fluid flows.

The data presented in figure 12 give insight into the critical applied field as a function of the applied field ratio β. The contour of $\langle \overline{C'^2} \rangle_{xy} = 0.002$ (shown as a bold solid line in figure 12) defines the critical applied field as a function of β. This critical applied field definition is consistent with our aforementioned definition of a doubling of the base state perturbation energy. In figure 12(a) the contour is nearly vertical for values roughly between 1.5 and 0.9, showing that the critical field is a weak function of β in this range. Outside of this range, the critical field increases rapidly and is a strong function of β (note the nearly horizontal regions of this contour). This dependence of the critical applied field on β can be related to the characteristic diffusion thicknesses over which strong conductivity gradients occur. When the centre or the sheath stream widths are of the order of the spanwise diffusion thickness, the conductivity gradient is rapidly homogenized by diffusion. These conditions result in a reduction in the maximum conductivity gradient for the cases of $h/\delta \leqslant 1$ (small centre stream width) and $(w-h)/\delta \leqslant 1$ (small sheath stream width). We can predict when these conditions are satisfied using equation (5.1), the experimentally measured relationship between the centre stream width h and the applied field ratio, β. Although the relationship between h and β describes the width of the fluorescent scalar dye in the centre stream, we can assume it approximately characterizes the initial upstream width of the high-conductivity stream as well. The definition of h that we use in § 3 is relatively independent of the diffusion thickness for $h/\delta > 1$. Additionally, in the upstream region, the relation between h and β is dependent mostly on the conductivity ratio γ and the channel electro-osmotic mobility. We estimate the diffusive length scale δ with equation (3.14) as $\delta = 6\,\mu\text{m}$ at a downstream location of $x/w = 1.5$. This estimate uses the effective diffusivity of KCl (see table 2), and an electro-osmotic

velocity of $3\,\mathrm{mm\,s^{-1}}$ at $E_a = 400\,\mathrm{V\,cm^{-1}}$. We choose the $x/w = 1.5$ location because it is the approximate location of maximum perturbation intensity for critical applied field conditions. For $\gamma = 100$, the conditions of thin centre stream ($h/\delta \leqslant 1$) and thin sheath streams ($(w-h)/\delta \leqslant 1$) are satisfied for $\beta \geqslant 1.47$ and $\beta \leqslant 0.94$, respectively. Figure 12(a) shows that the critical applied field required for instability does indeed become a strong function of β and dramatically increases outside of the range $0.94 < \beta < 1.47$.

Next, we can show that our scaling analyses provide a good prediction of the trends observed for critical applied field value as a function of both β and γ. We first relate β to the centre stream width h using equations (5.1) and (5.2). We then use the factor $\nabla^*\sigma^*|_{max}$ in equation (3.19) to estimate the value of the maximum conductivity field gradient for a given centre width h, sheath width $(w-h)$, and diffusion thickness δ. Combining equations (5.1), (5.2) and (3.19), we can plot contours of $Ra_{e,\ell} = 205$ as a function of the nominally applied field and field ratio. The results of the scaling analysis prediction are shown as a bold dashed contour in figure 12. The simple first-order scaling relation of modified electric Rayleigh numbers is shown to agree well with the experimentally observed trends in the critical applied field as a function of the applied field ratio β and γ. The maximum conductivity gradient function $\nabla^*\sigma^*|_{max}$ forces the contour of constant Rayleigh number to bend towards higher applied fields as the centre and sheath stream widths approach the diffusion thickness. In all cases, the largest conductivity gradients are limited by the smallest diffusive length scale allowed by each value of β. Overly thin centre streams (small β) and sheath streams (larger β) are quickly dissipated by molecular diffusion.

As a whole, the scaling analyses show that the critical conditions for the onset of flow instability are a result of the competing effects of electroviscous stretching and folding of conductivity interfaces and the dissipative effect of molecular diffusion. The electroviscous motion is a result of the balance between electrical body forces and viscous forces in the bulk liquid. We further show that the net charge scales with the maximum conductivity gradients which are a function of geometry, boundary conditions and the effects of molecular diffusion.

5.9. *Spectral analysis*

We quantify the wavenumber energy distribution of the instability disturbances by spatial energy spectra. The spectra are obtained from ensemble-averaged discrete fast Fourier transforms of instantaneous scalar images. The spatial fluctuation transforms are performed on intensity profiles that are vertical averages of a rectangle of 3 pixels along the vertical direction and 500 long. These subregions are extracted from the instantaneous images along the x-axis centreline ($y/w = 0$) from $x/w = 0$ to 16.5. We apply a Hanning window to reduce wavenumber leakage and normalize the spectra by the area average scalar perturbation $\langle \overline{C'^2} \rangle_{xy}$. Figure 16 shows a contour map of spatial energy spectra as a function of normalized wavenumber $k = 2w/\lambda$ and a range of applied fields at $\gamma = 100$, $\beta = 1.26$. Below the critical field, $E_a < 365\,\mathrm{V\,cm^{-1}}$, there is a single d.c. peak at low wavenumbers. This near-d.c. peak is due to the finite resolution of this finite-duration Fourier transform and the effect of the Hanning window. At the critical applied field of $365\,\mathrm{V\,cm^{-1}}$, a strong peak forms centred at $k = 1$ and a weaker peak at $k = 2$. The wavenumber of this dominant peak decreases with applied field, showing that the wavelength of scalar structures increases with increasing field. At much higher applied fields we see a continuous slowly decaying spectrum.

Figure 17 shows three sample spectra extracted from figure 16 at the applied fields: $E_a = 360$, 388 and $888\,\mathrm{V\,cm^{-1}}$. At $E_a = 360\,\mathrm{V\,cm^{-1}}$, the flow is stable and the spectra shows a decrease from the d.c. peak value from $k = 0.1$ to about 0.2. For

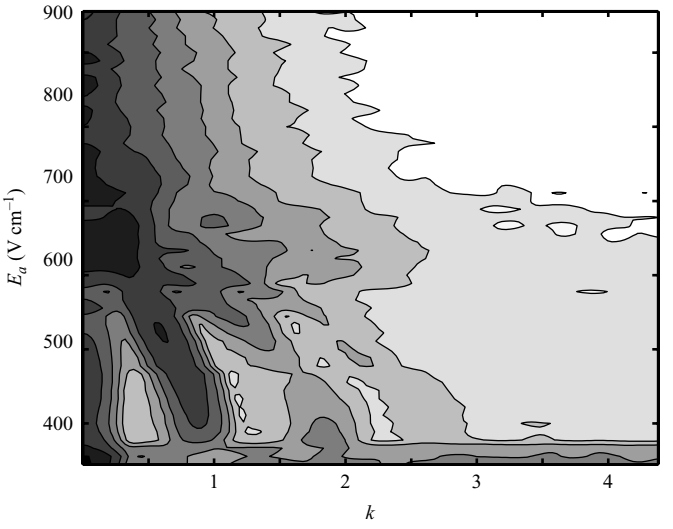

FIGURE 16. A scalar spatial energy spectra intensity contour map plotted as a function of dimensionless wavenumber, $k = 2w/\lambda$ and nominal applied field, E_a for $\gamma = 100$ and $\beta = 1.26$. The contours are spaced by 0.5 and are defined as $\log(\overline{\widehat{C(x)}\widehat{C(x)}^*})/\langle\overline{C'^2}\rangle_{xy}$, where the overbar denotes ensemble averaging over 200 spatial spectra. At low fields, energy is limited to near-zero wave-numbers. At the critical applied field of 365 V cm^{-1}, a strong peak forms centred at $k = 1$ and a weaker harmonic at $k = 1.9$. The wavenumber of this dominant peak decreases with applied field, showing that the wavelength of scalar structures increases with increasing field. At applied fields above about 750 V cm^{-1}, we observe a continuous slowly decaying spectrum.

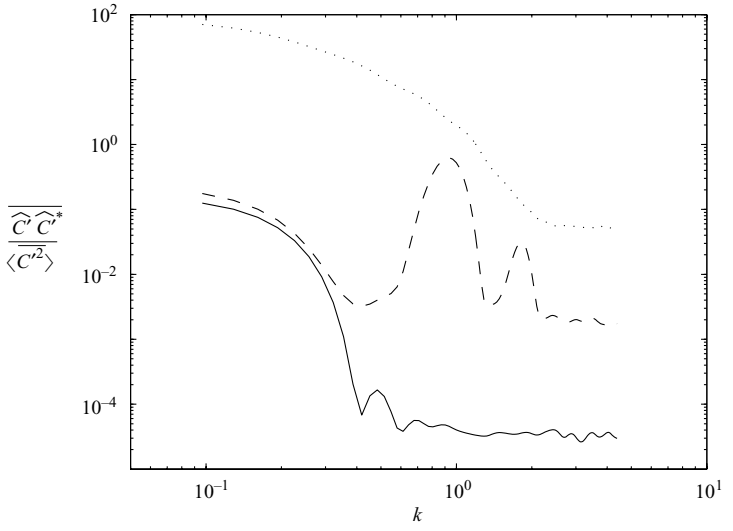

FIGURE 17. Selected scalar spatial energy spectra plotted as a function of dimensionless wave number, $k = 2w/\lambda$ for $\gamma = 100$, $\beta = 1.26$, and three applied fields. At $E_a = 360$ V cm^{-1} (——) the flow is stable and there is sharp decrease in energy from d.c. Above the critical applied field, $E_a = 388$ V cm^{-1} (– – –), there is a strong peak at $k = 1$ and a weaker harmonic at $k = 2$. The peak at $k = 1$ shows the dominant disturbance wavelength is nearly equal to the channel width. At higher applied fields, $E_a = 888$ V cm^{-1} ($\cdots$), we obtain an energy spectrum that cascades continuously over three decades. The continuous spectral decay in energy is due to the effects of electroviscous velocity fluctuations and molecular diffusion on the scalar field. Spectra are separated in the vertical direction for improved clarity.

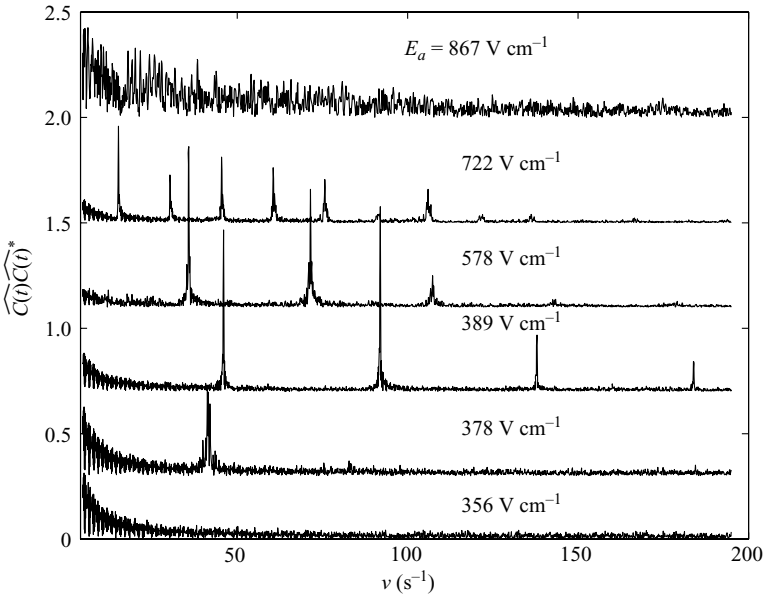

FIGURE 18. Scalar temporal power spectra for $\gamma = 100$, $\beta = 1.26$, and measured at $x/w = 3$ and $y/w = 0$ at the applied fields noted above each curve. The hat in the ordinant label denotes a discrete Fourier transform and the asterisk denotes a complex conjugate. The spectra are displaced in the vertical direction for improved clarity (although the same scale is used for all of the traces). When the flow is stable there is only a broad d.c. peak near $\nu = 0\,\mathrm{s}^{-1}$. For the marginally unstable flow, $E_a = 378\,\mathrm{V\,cm}^{-1}$, a single narrow peak forms at $\nu = 42\,\mathrm{s}^{-1}$ which is consistent with a nearly sinuous disturbance. At $E_a = 389\,\mathrm{V\,cm}^{-1}$, the fundamental frequency shifts towards a higher frequency of $\nu = 42.25\,\mathrm{s}^{-1}$ and weaker harmonics form at 88.5, 132.75 and $177\,\mathrm{s}^{-1}$. The shift to higher frequencies is consistent with a first-order increase in the electro-osmotic velocity and a slowly varying spatial wavenumber. At higher fields, $E_a = 722\,\mathrm{V\,cm}^{-1}$, we observe a bifurcation and period doubling. At $E_a = 867\,\mathrm{V\,cm}^{-1}$, we observe a continuous energy spectra.

fields in excess of the critical value, $E_a = 388\,\mathrm{V\,cm}^{-1}$, there is a strong peak at $k = 1$ and a weaker harmonic at $k = 2$. These peaks show that the dominant disturbance length scale is approximately equal to the channel width $2w$. This is confirmed by a visual inspection of the coherent structures in figure 4(*c*). At much higher fields of $E_a = 888\,\mathrm{V\,cm}^{-1}$, we obtain an energy spectrum that cascades continuously over three decades. This spectra shows a near power-law behaviour for wavenumbers in the range of $k = 0.5$ to 3. The decay is due to the dissipation of small-scale concentration field fluctuations by electroviscous stirring and diffusive dissipation. Electric body forces and electroviscous velocity fluctuations play a role analogous to inertia and turbulent eddies in turbulent flow (see Batchelor 1959).

Lastly, we can also calculate temporal scalar power spectra from time records generated from a set of extended image series (experiment 41 in table 3). The data sets contain 2000 images that are 3 pixels in the vertical direction and 512 pixels long. These data sets are recorded at 390 frames per second. We also performed additional experiments at selected high field conditions with image frame rates of 25, 50, 115 and 250 frames per second and compared spectral and temporal content to verify that data were not aliased. Time series records are composed of the area averaged intensity of a 3×3 pixel region centred along the x-axis at $y/w = 0$. We again apply a Hanning window to reduce frequency leakage. Figure 18 shows six temporal spectra calculated at $\gamma = 100$, $\beta = 1.26$, and six applied fields. At $E_a = 356\,\mathrm{V\,cm}^{-1}$, the flow is stable and there is only a d.c. peak near $\nu = 0\,\mathrm{s}^{-1}$ (broadened by the

finite resolution and the effect of the Hanning window). For a marginally unstable flow at $E_a = 378\,\mathrm{V\,cm^{-1}}$, a single narrow peak forms at $\nu = 42\,\mathrm{s^{-1}}$. A single peak is consistent with a nearly sinuous disturbance as visualized in figure 4(*b*). With a small increase in the applied field to $E_a = 389\,\mathrm{V\,cm^{-1}}$, the fundamental frequency shifts toward a higher value of $\nu = 44.25\,\mathrm{s^{-1}}$ and weaker harmonics form at 88.5, 132.75 and $177\,\mathrm{s^{-1}}$. The shift to higher frequencies is consistent with a first-order increase in the electro-osmotic velocity and a spatial wavenumber weakly dependent on the field in this region. At higher fields, the fundamental frequency peak and associated harmonic frequencies shift to lower frequency values owing to a now significantly decreasing spatial wavenumber. We observe a bifurcation and period doubling at $E_a = 722\,\mathrm{V\,cm^{-1}}$. At $E_a = 867\,\mathrm{V\,cm^{-1}}$, we observe a continuous energy spectra consistent with the results showed for spatial energy spectra. Bifurcations, period doubling, and continuous energy spectra are common to nonlinear chaotic systems and we will further investigate these characteristics of the strong nonlinear behaviour of EKI in a future publication.

6. Conclusions

Electrokinetic instabilities are generated by the formation of net electrical charge in bulk liquid regions outside the electric double layer. This net charge is formed in regions of the flow where the local conductivity gradient and electric field are parallel. The total (internally generated plus external) electric field couples with charge density to generate electrical body forces that are balanced by viscosity. This force balance generates velocity fluctuations with a magnitude described by the electrovicous velocity scale. Electrokinetic flows with conductivity gradients become unstable when the destabilizing effects of electroviscous stretching and folding of conductivity interfaces dominates over the dissipative effects of molecular diffusion.

We have presented a parametric experimental study of convective EKI in isotropically etched cross-shaped microchannels using quantitative epifluorescence imaging. We perform the experiments in a configuration that is similar to the primary step of a pinched-flow electrokinetic injection where the centre stream and sheath flows have mismatched ionic conductivities. We explore variations of applied d.c. electric field, electric field ratio, and centre-to-sheath conductivity ratios, and these impose variations of the electric Rayleigh number across four orders of magnitude.

We have shown that EKI in an electrokinetic focusing-type flow in a cross-shaped channel intersection leads to coherent scalar structures in the outlet channel. These structures are sinuous for $\gamma > 1$ (higher centre stream conductivity) and $\gamma < 1$ dilational for (smaller centre stream conductivity). When the applied field exceeds a critical value, perturbations in the scalar field grow exponentially in space. The origin of disturbances moves upstream with increasing field. For supercritical applied fields and large conductivity ratios ($\gamma \geqslant 8$), disturbances grow rapidly from the origin of the conductivity interfaces ($x/w = 0$). This behaviour suggests that the magnitude of the local electroviscous velocity produced by electric body forces is of the same order as the advective velocity provided by electroosmosis.

We use quantitative interpretation of experimental results to show that the critical electric field required for instability depends on both the centre-to-sheath conductivity ratio γ and the applied field ratio β which determines the width of the centre stream. We show that the charge density (in the bulk fluid outside the electric double layer) and the local Rayleigh number scale with the maximum conductivity gradients in the flow. This conductivity gradient is a function of the conductivity ratio, the centre stream width, and the diffusive length scale over which conductivity gradients occur.

We introduce a modified local electric Rayleigh number and show that the flow becomes unstable at a critical electric Rayleigh number ($Ra_{e,\ell} = 205$) for a wide range of conductivity ratios γ (three orders of magnitude) and applied field ratios β. Future work may include a detailed investigation of the explicit dependence of the electric Rayleigh number on each of the pertinent length scales in the flow (including d, w, h and δ), which requires a set of experiments where each of these scales can be varied independently.

Finally, spatial energy spectra show that the dominant disturbance wavelengths are commensurate and scale with the channel height ($2w$) for unstable flows near the critical applied field. At higher fields, the spatial spectra cascade continuously over a decade of wavenumbers. Temporal spectra show that the initial disturbances are purely sinuous with a strong fundamental frequency. At higher applied fields, the flow develops additional harmonics and there is clear evidence of bifurcation and period doubling with increasing electric field. We are continuing to explore the rich and dynamic behaviour of these electrokinetic flows.

This work was sponsored by an NSF PECASE Award (J.G.S., award number CTS-0239080-001) with Dr Michael W. Plesniak as grant monitor. J.D.P. thanks Michael H. Oddy, Rajiv Bharadwaj and Hao Lin for insightful discussions.

Appendix. Derivation of $\nabla^*\sigma^*|_{max}$

The generalized equation for the spanwise diffusion of an initially top-hat scalar profile of conductivity is given in equation (3.16). The conductivity gradient is given by the first spatial derivative of equation (3.16), given as,

$$\begin{aligned}\nabla^*\sigma^* = \frac{\mathrm{d}\sigma^*}{\mathrm{d}(y/\delta)} \;=\; & \exp\left(-\left(\frac{y+h}{2\delta}\right)^2\right) - \exp\left(-\left(\frac{y-h}{2\delta}\right)^2\right) \\ & + \exp\left(-\left(\frac{y+h-2w}{2\delta}\right)^2\right) - \exp\left(-\left(\frac{y-h-2w}{2\delta}\right)^2\right) \\ & + \exp\left(-\left(\frac{y+h+2w}{2\delta}\right)^2\right) - \exp\left(-\left(\frac{y-h+2w}{2\delta}\right)^2\right), \quad \text{(A 1)}\end{aligned}$$

where we have approximated the expression with a truncation at $n = 2$ and normalized by $2/\sqrt{3}$. The first two terms account for gradients due to the diffuse top-hat distribution, and the final four terms account for the first set of reflections at $y = \pm w$. Figure 19 shows profiles of normalized conductivity, σ^*, and conductivity gradient, $\nabla^*\sigma^*$, for a diffusion thickness of $\delta/w = 0.1$ and three different values of the normalized centre stream width $h/w = 0.1$, 0.5 and 0.9. For $h/w = 0.5$, the top-hat profile spans half of the total channel width and the maximum normalized conductivity gradient is equal to unity. When the centre stream width is equal to, or smaller than, the diffusive length scale ($h/\delta \leqslant 1$), then the maximum conductivity ratio is decreased, as shown for $h/w = 0.1$ in figure 19. Similarly, the maximum gradient is again reduced when the sheath stream width is equal to or smaller than the diffusive length scale ($(w-h)/\delta \leqslant 1$), as shown for $h/w = 0.9$.

Next, we derive a compact analytical expression for maximum normalized conductivity gradients that occur in one-dimensional diffusion along the spanwise direction. The exact solution for the maximum conductivity gradients are obtained by evaluating the untruncated form of equation (A 1) at the roots of the second conductivity derivative $\mathrm{d}^2\sigma^*/\mathrm{d}(y/\delta)^2$. Since we are interested in a compact and

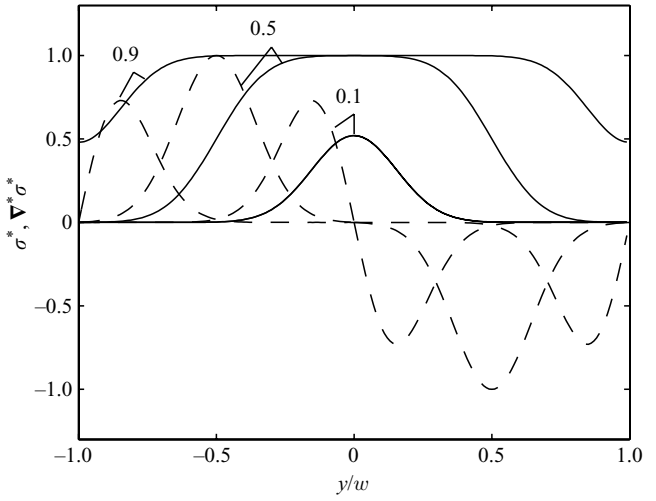

FIGURE 19. Spanwise normalized conductivity σ^* (——) and conductivity gradient $\nabla^*\sigma^*$ (– – –) for $\delta/w = 0.1$ and $h/w = 0.1$, 0.5 and 0.9. For thin centre streams ($h/w = 0.1$), the maximum conductivity value and gradients are reduced and the centre stream is nearly equal to the diffusion thickness ($h/\delta = 1$). For wide centre streams ($h/w = 0.9$), the sheath streams are nearly equal to the diffusion thickness ($(w-h)/\delta = 1$) and the maximum conductivity gradients are again reduced.

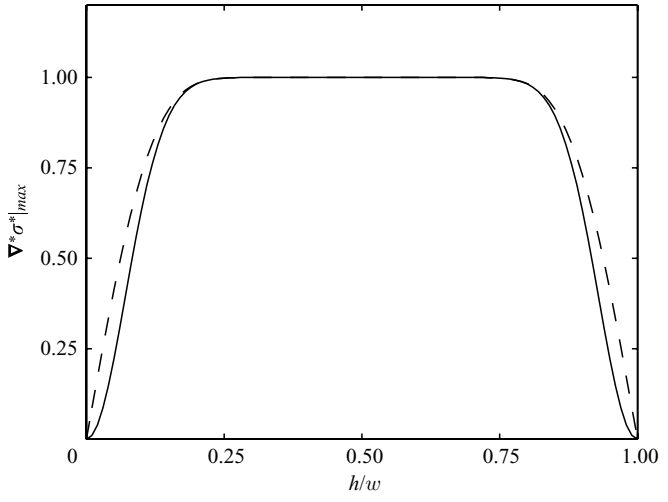

FIGURE 20. Maximum normalized value of spanwise conductivity gradient plotted as a function of the centre stream width h/w for $\delta/w = 0.1$. We plot the exact solution $|\mathrm{d}\sigma^*/\mathrm{d}(y/\delta)|_{max}$ (– – –) and the approximate solution $\nabla^*\sigma^*|_{max}$ (——). There is a reduction in the maximum conductivity gradient when the centre stream is thin compared to the diffusion thickness ($h/\delta \leqslant 1$). The gradient is also reduced when the sheath stream is small compared to the diffusion thickness ($(w-h)/\delta \leqslant 1$).

approximate solution, we evaluate equation (A 1) at $y = -h$ (which results in a positive gradient), given as,

$$\nabla^*\sigma^*\Big|_{max} = \frac{\mathrm{d}\sigma^*}{\mathrm{d}(y/\delta)}\Big|_{max} = 1 - \exp\left(-\left(\frac{h}{\delta}\right)^2\right) - \exp\left(-\left(\frac{w-h}{\delta}\right)^2\right), \qquad (A\,2)$$

where terms of the order of $\exp -((w/\delta)^2)$ and smaller have been dropped. Figure 20 shows a comparison of the exact solution for $\mathrm{d}\sigma^*/\mathrm{d}(y/\delta)|_{max}$, where the roots of

$d^2\sigma^*/d(y/\delta)^2$ are obtained numerically using the Ridder method, and the $\nabla^*\sigma^*|_{max}$ approximation above evaluated at $y = -h$. The maximum normalized conductivity gradients are shown as a function of the normalized centre stream width h/w with an initial diffusion thickness of $\delta/w = 0.1$. The maximum normalized conductivity gradients are equal to unity for a wide range of the centre stream thicknesses, $0.2 < h/w < 0.8$. Outside of this range the maximum gradients are reduced because the centre or sheath flow stream widths are equal to, or smaller than, the diffusive length scale. For the conditions of interest here, the $y = -h$ approximation generates errors for $d\sigma^*/d(y/\delta)|_{max}$ of less than 20% of the full range.

REFERENCES

Adrian, R. J. 1991 Particle-imaging techniques for experimental fluid mechanics. *Annu. Rev. Fluid Mech.* **23**, 261–304.

Batchelor, G. K. 1959 Small-scale variation of convected quantities like temperature in turbulent fluid. Part 1. General discussion and the case of small conductivity. *J. Fluid Mech.* **5**, 113–133.

Baygents, J. C. & Baldessari, F. 1998 Electrohydrodynamic instability in a thin fluid layer with an electrical conductivity gradient. *Phys. Fluids* **10**, 301–311.

Bénard, H. 1908 *C. R. Acad. Sci. Paris* **839**, 147.

Bharadwaj, R. & Santiago, J. 2005 Dynamics of field amplified sample stacking. *J. Fluid Mech.* **543**, 57–92.

Bruin, G. J. M. 2000 Recent developments in electrokinetically driven analysis on microfabricated devices. *Electrophoresis* **21**, 3931–3951.

Burgi, D. S. & Chien, R. L. 1991 Optimization in sample stacking for high-performance capillary electrophoresis. *Analyt. Chem.* **63**, 2042–2047.

Chen, C.-H., Lin, H., Lele, S. K. & Santiago, J. G. 2005 Convective and absolute electrokinetic instability with conductivity gradients. *J. Fluid Mech.* **524**, 263–303.

Crank, J. 1975 *Mathematics of Diffusion*, 2nd edn. Oxford University Press.

Cummings, E. B. 2000 An image processing and optimal nonlinear filtering technique for particle image velocimetry of microflows. *Exp. Fluids* **29**, S42–S50.

Dang, F. Q., Zhang, L. H., Jabasini, M., Kaji, N. & Baba, Y. 2003 Characterization of electrophoretic behavior of sugar isomers by microchip electrophoresis coupled with videomicroscopy. *Analyt. Chem.* **75**, 2433–2439.

Devasenathipathy, S. 2003 Particle imaging diagnostics and stacking dynamics in microfluidic systems. PhD thesis.

Devasenathipathy, S. & Santiago, J. 2005 *Microscale Diagnostic Techniques*, chap. Electrokinetic Flow Diagnostics. Springer.

Devasenathipathy, S., Santiago, J. G. & Takehara, K. 2002 Particle tracking techniques for electrokinetic microchannel flows. *Analyt. Chem.* **74**, 3704–3713.

Ghosal, S. 2004 Fluid mechanics of electro-osmotic flow and its effect on band broadening in capillary electrophoresis. *Electrophoresis* **25**, 214–28.

Harrison, D. J., Manz, A., Fan, Z. H., Ludi, H. & Widmer, H. M. 1992 Capillary electrophoresis and sample injection systems integrated on a planar glass chip. *Analyt. Chem.* **64**, 1926–1932.

Herr, A. E., Molho, J. I., Drouvalakis, K. A., Mikkelsen, J. C., Utz, P. J., Santiago, J. G. & Kenny, T. W. 2003 On-chip coupling of isoelectric focusing and free solution electrophoresis for multidimensional separations. *Analyt. Chem.* **75**, 1180–1187.

Hoburg, J. F. & Melcher, J. R. 1976 Internal electrohydrodynamic instability and mixing of fluids with orthogonal field and conductivity gradients. *J. Fluid Mech.* **73**, 333–351.

Huang, X., Gordon, M. J. & Zare, R. N. 1988 Current-monitoring method for measuring the electro-osmotic flow rate in capillary zone electrophoresis. *Analyt. Chem.* **60**, 1837–1838.

Huerre, P. & Monkewitz, P. A. 1990 Local and global instabilities in spatially developing flows. *Annu. Rev. Fluid Mech.* **22**, 473–537.

Hunter, R. J. 1981 *Zeta Potential in Colloid Science*. Academic.

Inoué, S. & Spring, K. 1997 *Video Microscopy: The Fundamentals*. Plenum.

Jain, R., Sharma, N. & Bhargava, M. 2003 Electrochemical degradation of rhodamine b dye in textile and paper industries effluent. *J. Sci. Indust. Res.* **62**, 1138–1144.

von Kármán, T. 1912 *Gött. Nachr*.

Kirby, B. J. & Hasselbrink, E. F. 2004 Zeta potential of microfluidic substrates: 1. theory, experimental techniques, and effects on separations. *Electrophoresis* **25**, 187–202.

Koochesfahani, M., Cohn, R. & McKinnon, C. 2000 Simultaneous whole-field measurements of velocity and concentration fields using a combination of mtv and lif. *Meas. Sci. Technol.* **11**, 1289–300.

Lide, D. (ed.) 1997 *CRC Handbook of Chemistry and Physics*, 77th edn. CRC Press.

Lin, H., Storey, B. D., Oddy, M. H., Chen, C. H. & Santiago, J. G. 2004 Instability of electrokinetic microchannel flows with conductivity gradients. *Phys. Fluids* **16**, 1922–1935.

Locascio, L. E. 2004 Microfluidic mixing. *Analyt. Bioanalyt. Chem.* **379**, 325–327.

Manz, A., Graber, N. & Widmer, H. M. 1990 Miniaturized total chemical-analysis systems – a novel concept for chemical sensing. *Sensors Actuators* B *Chem.* **1**, 244–248.

Meinhart, C. D., Wereley, S. T. & Santiago, J. 1999 PIV measurements of a microchannel flow. *Exps. Fluids* **27**, 414–419.

Melcher, J. R. & Taylor, G. I. 1969 Electrohydrodynamics – a review of role of interfacial shear stresses. *Annu. Rev. Fluid Mech.* **1**, 111–146.

Oddy, M. H. & Santiago, J. G. 2005 A multiple-species model for electrokinetic instability. *Phys. Fluids* **17**, 064108.

Oddy, M. H., Santiago, J. G. & Mikkelsen, J. C. 2001 Electrokinetic instability micromixing. *Analyt. Chem.* **73**, 5822–5832.

O'Donnell, B., Chen, J. N. & Lin, S. P. 2001 Transition from convective to absolute instability in a liquid jet. *Phys. Fluids* **13**, 2732–2734.

Posner, J. D. & Santiago, J. G. 2004 Convective electrokinetic flow instabilities in a cross-shaped microchannel. In *Eighth International Conference on Miniaturized Systems in Chemistry and Life Sciences* (ed. T. Laurell, J. Nilsson, K. J. D. Harrison & J. Kutter), vol. 1, pp. 623–625. The Royal Society of Chemistry, Malmo, Sweden.

Probstein, R. F. 1994 *Physicochemical Hydrodynamics*, 2nd edn. Wiley.

Ramsey, J. M. 2001 Preface. In *Micro Total Analysis Systems*. Kluwer.

Ren, C. L. & Li, D. Q. 2004 Effects of spatial gradients of electrical conductivity on chip-based sample injection processes. *Analytic Chim. Acta* **518**, 59–68.

Ren, L. Q., Escobedo, C. & Li, D. 2001 Electro-Osmotic flow in a microcapillary with one solution displacing another solution. *J. Colloid Interface Sci.* **242**, 264–271.

Rhodes, P. H., Snyder, R. S. & Roberts, G. O. 1989 Electrohydrodynamic distortion of sample streams in continuous-flow electrophoresis. *J. Colloid Interface Sci.* **129**, 78–90.

Sadr, R., Yoda, M., Zheng, Z. & Conlisk, A. T. 2004 An experimental study of electro-osmotic flow in rectangular microchannels. *J. Fluid Mech.* **506**, 357–367.

Santiago, J. G. 2001 Electro-osmotic flows in microchannels with finite inertial and pressure forces. *Analyt. Chem.* **73**, 2353–2365.

Santiago, J. G., Wereley, S. T., Meinhart, C. D., Beebe, D. J. & Adrian, R. J. 1998 A particle image velocimetry system for microfluidics. *Exps. Fluids* **25**, 316–319.

Saville, D. A. 1997 Electrohydrodynamics: the Taylor–Melcher leaky dielectric model. *Annu. Rev. Fluid Mech.* **29**, 27–64.

Scales, P. J., Grieser, F., Healy, T. W., White, L. R. & Chan, D. Y. C. 1992 Electrokinetics of the silica solution interface – a flat-plate streaming potential study. *Langmuir* **8**, 965–974.

Shah, R. & London, A. 1978 *Laminar Flow Forced Convection in Ducts*, 2nd edn. Academic.

Shin, S. M., Kang, I. S. & Cho, Y.-K. 2005 Mixing enhancement by using electrokinetic instability under time-periodic electric field. *J. Micromech. Microengng.* **15**, 455–462.

Shultz-Lockyear, L. L., Colyer, C. L., Fan, Z. H., Roy, K. I. & Harrison, D. J. 1999 Effects of injector geometry and sample matrix on injection and sample loading in integrated capillary electrophoresis devices. *Electrophoresis* **20**, 529–538.

Sinton, D. & Li, D. Q. 2003 Electro-osmotic velocity profiles in microchannels. *Colloids Surfaces* A *Physicochem. Engng Aspects* **222**, 273–283.

Stone, H. A., Stroock, A. D. & Ajdari, A. 2004 Engineering flows in small devices: microfluidics toward a lab-on-a-chip. *Annu. Rev. Fluid Mech.* **36**, 381–411.

Storey, B. D., Tilley, B., Lin, H. & Santiago, J. G. 2005 Electrokinetic instabilities in thin microchannels. *Phys. Fluids* **17**.

Szymczyk, A., Fievet, P., Aoubiza, B., Simon, C. & Pagetti, J. 1999 An application of the space charge model to the electrolyte conductivity inside a charged microporous membrane. *J. Membrane Sci.* **161**, 275–285.

Thormann, W., Mosher, R. A. & Bier, M. 1986 Experimental and theoretical dynamics of isoelectric focusing elucidation of a general separation mechanism. *J. Chromatography* **351**, 17–30.

Tokumaru, P. T. & Dimotakis, P. E. 1995 Image correlation velocimetry. *Exps. Fluids* **19**, 1–15.

Vilkner, T., Janasek, D. & Manz, A. 2004 Micro total analysis systems. recent developments. *Analyt. Chem.* **76**, 3373–3385.

Yao, S. H., Hertzog, D. E., Zeng, S. L., Mikkelsen, J. C. & Santiago, J. G. 2003 Porous glass electro-osmotic pumps: design and experiments. *J. Colloid Interface Sci.* **268**, 143–153.